

Node-Dependent Kinematics Approach for Damage Analysis of Reinforced Concrete Structures

Original

Node-Dependent Kinematics Approach for Damage Analysis of Reinforced Concrete Structures / Shen, J.; Arruda, M. R.; Pagani, A.; Carrera, E.; Zappino, E.; Augello, R.; Petrolo, M.. - In: JOURNAL OF STRUCTURAL ENGINEERING. - ISSN 0733-9445. - 151:8(2025). [10.1061/JSENDH.STENG-13729]

Availability:

This version is available at: 11583/3000438 since: 2025-05-27T06:55:56Z

Publisher:

ASCE

Published

DOI:10.1061/JSENDH.STENG-13729

Terms of use:

This article is made available under terms and conditions as specified in the corresponding bibliographic description in the repository

Publisher copyright

ASCE postprint/Author's Accepted Manuscript

This material may be downloaded for personal use only. Any other use requires prior permission of the American Society of Civil Engineers. This material may be found at <http://dx.doi.org/10.1061/JSENDH.STENG-13729>.

(Article begins on next page)

Node-dependent kinematics approach for damage analysis of reinforced concrete structures

Jiahui Shen¹, Mário Rui Arruda², Alfonso Pagani ^{*}³, Erasmo Carrera⁴,
Enrico Zappino⁵, Riccardo Augello⁶, and Marco Petrolo⁷

¹PhD student, *Mul2* Lab, Department of Mechanical and Aerospace Engineering, Politecnico di
Torino, Torino, 10129, Italy; email: jiahui.shen@polito.it

²Research Associate, CERIS, Instituto Superior Técnico, Universidade de Lisboa, Lisboa,
1049-001, Portugal; email: mario.rui.arruda@edu.ulisboa.pt

³Full Professor, *Mul2* Lab, Department of Mechanical and Aerospace Engineering, Politecnico di
Torino, Torino, 10129, Italy; email: alfonso.pagani@polito.it (Corresponding author)

⁴Full Professor, *Mul2* Lab, Department of Mechanical and Aerospace Engineering, Politecnico di
Torino, Torino, 10129, Italy; email: erasmo.carrera@polito.it

⁵Associate Professor, *Mul2* Lab, Department of Mechanical and Aerospace Engineering,
Politecnico di Torino, Torino, 10129, Italy; email: enrico.zappino@polito.it

⁶Assistant Professor, *Mul2* Lab, Department of Mechanical and Aerospace Engineering, Politecnico
di Torino, Torino, 10129, Italy; email: enrico.zappino@polito.it

⁷Associate Professor, *Mul2* Lab, Department of Mechanical and Aerospace Engineering,
Politecnico di Torino, Torino, 10129, Italy; email: enrico.zappino@polito.it

Abstract: Modeling damage behavior in engineering structures is vital, but balancing computational efficiency and accuracy presents a significant challenge. This study introduces an advanced higher-order beam model incorporating a node-dependent kinematics approach, enhancing the efficiency of damage analysis in reinforced concrete structures. The proposed beam model is built in the framework of Carrera Unified Formulation, enabling a three-dimensional displacement field from a one-dimensional beam model via variable cross-sectional

*

26 expansion functions. The node-dependent kinematics approach allows diverse cross-sectional
27 kinematics at different nodes on the same beam element. Therefore, a customized approach
28 can be applied where critical areas susceptible to localized damage utilize Lagrange poly-
29 nomials and Component-Wise approach for detailed analysis, while non-critical zones apply
30 lower-order Taylor polynomials to reduce computational resources. The model incorporates
31 a modified Mazars damage model for concrete and Von Mises plasticity for steel. Four nu-
32 merical assessments show that the proposed beam model with node-dependent kinematics
33 can maintain accuracy while reducing degrees of freedom by 35% – 60% compared to fully
34 refined models with Lagrange polynomials. Moreover, the node-dependent kinematics only
35 require simple adjustments to the cross-sectional kinematics as necessary without extensive
36 mesh refinement. This scalability significantly simplifies the tuning process of beam models
37 for practical applications.

38

39 1 Introduction

40 Over the past decades, numerous numerical models have been developed for the structural
41 analysis of Reinforced Concrete (RC) structures. Experimental studies (MacGregor et al.,
42 1997) have revealed that RC structures exhibit complex behavior, including concrete crack-
43 ing and crushing, steel plasticity, and the bond-slip interaction between steel rebars and
44 concrete. Capturing these phenomena in a numerical method demands significant compu-
45 tational resources. Despite the challenges posed by computational requirements, numerical
46 models are still essential in specialized engineering and for conducting parametric studies
47 (Kadhim et al., 2020), which provides a cost-efficient alternative to experimental testing. The
48 crucial aspect of simulating RC structures is choosing appropriate material representations
49 for concrete and steel according to specific application scenarios. Additionally, accurately
50 modeling the interaction between concrete and steel reinforcement remains a significant and
51 ongoing challenge (Ogura et al., 2008).

52 Currently, two principal approaches (Maekawa et al., 2003) are widely utilized in the
53 simulation of RC structures: the continuum method employing three-dimensional (3D) Finite
54 Element Analysis (FEA) and the frame modeling method. The FEA with continuum method

55 employs 3D solid elements to model concrete, whereas steel rebars are simulated using one-
56 dimensional (1D) beam or truss elements (Earij et al., 2017; Sinaei et al., 2012). Various
57 plasticity theories are applied to capture the behavior of steel rebars (de Souza Neto et al.,
58 2011). Continuum damage models, both isotropic (Mazars, 1984) and anisotropic (Halm and
59 Dragon, 1996), have been proposed and validated for concrete damage behavior. The bond-
60 slip interaction between concrete and steel is addressed by incorporating specialized elements
61 like contact or interface elements (Murcia-Delso and Benson Shing, 2015; Casanova et al.,
62 2012). Although this method achieves reliable accuracy, it demands substantial computational
63 resources, particularly for large-scale structures such as RC bridges (Babazadeh et al., 2015)

64 Unlike the continuum method, frame elements, including lumped and distributed plasticity
65 methods, are more attractive due to their reduced computational requirements. Among these,
66 the fiber beam element is the most preferred for studying the seismic behavior of RC struc-
67 tures (Taucer et al., 1991; Spacone et al., 1996). In this approach, the section is discretized
68 into multiple fibers, and uniaxial constitutive relations govern each fiber according to materi-
69 als. Such a method allows for the independent modeling of the nonlinear behavior of concrete
70 and steel. The longitudinal behavior is commonly integrated with the Euler-Bernoulli beam
71 theory, where the shear deformations are neglected (Spacone et al., 1996). Then, the behav-
72 ior of the entire RC member can be approximated by a limited number of beam elements
73 through standard FE approaches. Notably, it has been reported that a single force-based
74 element can effectively simulate the nonlinear response of a frame member (Neuenhofer and
75 Filippou, 1997). Several approaches have been proposed to include the flexure-shear interac-
76 tion in the beam-column elements, reviewed in (Ceresa et al., 2007). The first way involves
77 the introduction of shear springs at the end of the element, which is simple and easy for im-
78 plementation but involves calibrating parameters (D’Ambrisi and Filippou, 1999; Marini and
79 Spacone, 2006). The second method consists of integrating Timoshenko beam theory into the
80 frame element and combined with multi-dimensional material constitutive laws, which ensure
81 the capture of flexure-shear interaction at both material and section levels. Different Timo-
82 shenko fiber beam elements have been proposed so far, including displacement-based (Ceresa
83 et al., 2009; Feng et al., 2017), force-based (Petrangeli et al., 1999; Mullapudi and Ayoub,

84 2013), and mixed formulation-based (Saritas and Filippou, 2009, 2013; Cheng and Shing,
85 2022). However, classical Timoshenko beam elements often have difficulties accurately cap-
86 turing nonlinear shear deformation due to the assumption of uniform shear stress or capturing
87 localized phenomena (Urmson and Mander, 2012; Girgin et al., 2018).

88 The trade-off between accuracy and computational demands is challenging. A potential
89 solution is represented by the higher-order beam theory based on Carrera Unified Formulation
90 (CUF) (Carrera et al., 2014). Within the framework of CUF, 1D beam models are employed to
91 describe the 3D displacement field by using various cross-sectional expansion functions. This
92 CUF-based beam theory provides a robust framework for overcoming limitations encountered
93 in classical beam models without relying on additional assumptions. These Euler-Bernoulli
94 and Timoshenko beam theories are considered particular cases by adjusting kinematics in
95 the CUF framework (Carrera et al., 2011). Compared to the previously mentioned frame
96 elements, a more accurate nonlinear shear effect can be taken into account by this CUF-based
97 beam model. Importantly, it provides 3D results comparable to those of 3D solid elements
98 while maintaining the efficiency of the 1D model, which makes it applicable to complex
99 structures such as these owning discontinuities. This capability is typically beyond the reach
100 of both lumped and distributed plasticity models. Moreover, 3D material constitutive laws are
101 directly employed for structural analysis rather than the requirement for the inelastic element
102 parameters, such as bending moment-curvature relationships in the lumped plasticity model.

103 The application of CUF-based higher-order beam theories has shown success in static
104 and dynamic analyses across various engineering structures (Carrera et al., 2022; Shen et al.,
105 2022). The Component-Wise (CW) approach, a recent development of CUF, considers the
106 exact geometry and material properties within the calculations. These models incorporating
107 the CW approach, referred to as refined CW models, are particularly beneficial for analyzing
108 composite structures such as RC structures (Carrera et al., 2022; Nagaraj and Maiaru, 2023).
109 In (Shen et al., 2023a), the CW models have demonstrated the capability to predict overall
110 softening behavior in RC beams without stirrups and to capture flexural failure in RC beams
111 with stirrups. However, some small beam elements, whose lengths are equal to the diameter of
112 the stirrups, are periodically employed to represent the stirrups' actual geometry accurately.

113 This exact representation of stirrups in RC structures demands increased beam element dis-
114 cretization, leading to a significant rise in Degrees of Freedom (DoFs) of refined CW models.
115 Furthermore, when dealing with areas of high-stress gradients, there is an increase in compu-
116 tational expense due to the need for more refined models. In the past, refined models were
117 employed across entire domains (Shen et al., 2023a), which is often unnecessary and leads to
118 computational inefficiencies, mainly when local effects are confined to small regions.

119 A more effective strategy involves applying the refined models only in the required regions,
120 whereas lower-order or classical models are employed in less critical areas. The challenge of
121 joining two different structural models with incompatible kinematics has been extensively ex-
122 plored, with numerous solutions detailed in (Carrera et al., 2018). In the present study, a new
123 Node-Dependent Kinematics (NDK) approach (Carrera and Zappino, 2017) is introduced in
124 the framework of CUF. This method allows the assignment of distinct kinematic assumptions
125 to different nodes within a single 1D beam element, enhancing accuracy in targeted regions
126 through refined kinematics. A transition element can connect the elements with different
127 kinematics, ensuring displacement continuity via the inherent shape functions in the Finite
128 Element (FE) formulation. The advantage of this approach is that the calculation is still
129 within the CUF framework, and no extra formulations are added, which is beneficial for com-
130 putational efficiency. Furthermore, the notable scalability of this method can avoid further
131 mesh refinement in FE models for global-local analysis (Carrera et al., 2019; Nagaraj et al.,
132 2023). Although the NDK approach has been previously applied to RC structures (Augello
133 et al., 2023), its use has been limited to linear analysis.

134 In this context, the current study aims to extend the NDK approach to the damage analysis
135 of RC structures in the framework of the 1D-CUF model. This study employs validated
136 material models, such as the modified Mazars damage model for concrete and Von Mises
137 plasticity for steel. These have demonstrated mesh-independent results in previous researches
138 (Shen et al., 2023b,c). The scope of investigation in this work is not only limited to RC beams
139 but also includes more complex engineering structures. To the authors' knowledge, it is the
140 first time to apply global-local strategies like the NDK approach to the nonlinear damage
141 analysis of RC structures. By employing the NDK approach, regions susceptible to critical

142 damage are modeled with higher refinement. In comparison, the lower class is applied to the
 143 rest, thereby saving computational costs while ensuring a relatively high accuracy. Hence, the
 144 proposed approach shows considerable potential for real-world engineering applications due
 145 to its scalability and the optimal balance between accuracy and computational efficiency.

146 **2 Unified higher-order beam models**

147 In the framework of CUF (Carrera et al., 2014), the 3D displacement field of 1D beam models
 148 can be derived using the cross-sectional expansion functions. In this work, the axial direction
 149 of a 1D beam model is denoted by y , and x and z represent the coordinates in the cross-
 150 sectional plane. Hence, the 3D displacement field of a beam-like structure is expressed as
 151 follows:

$$\mathbf{u}(x, y, z) = F_\tau(x, z)\mathbf{u}_\tau(y), \quad \tau = 1, 2, \dots, M \quad (1)$$

152 where $F_\tau(x, z)$ is the cross-sectional expansion function, $\mathbf{u}_\tau(y)$ denotes the vector of unknown
 153 displacements along the beam axis, τ is a summation notation, and M signifies the number
 154 of terms in the expansion functions. The selection of a particular expansion characterizes
 155 the capabilities of a structural model. Various options for $F_\tau(x, z)$ are thoroughly discussed
 156 in (Carrera et al., 2014). For the current analysis, both Taylor and Lagrange polynomial
 157 expansions are considered, and their details are provided in the subsequent sections.

158 **2.1 Taylor expansion models**

159 Taylor Expansions (TE) employ the Taylor-like polynomials, with base terms of the form
 160 $x^m z^n$, where m and n are positive integers. In general, kinematics based on TE can be named
 161 TE n , in which n indicates the order of Taylor-like polynomials. For instance, a second-
 162 order TE model (TE2) exploits a parabolic expansion of the Taylor-like polynomials, and the
 163 corresponding expansion expansions F_τ are:

$$F_1 = 1, \quad F_2 = x, \quad F_3 = z, \quad F_4 = x^2, \quad F_5 = xz, \quad F_6 = z^2 \quad (2)$$

164 Then, the 3D displacement field of the second-order TE model can be expressed explicitly:

$$\begin{aligned}
u_x(x, y, z) &= u_{x_1} + xu_{x_2} + zu_{x_3} + x^2u_{x_4} + xzu_{x_5} + z^2u_{x_6} \\
u_y(x, y, z) &= u_{y_1} + xu_{y_2} + zu_{y_3} + x^2u_{y_4} + xzu_{y_5} + z^2u_{y_6} \\
u_z(x, y, z) &= u_{z_1} + xu_{z_2} + zu_{z_3} + x^2u_{z_4} + xzu_{z_5} + z^2u_{z_6}
\end{aligned} \tag{3}$$

165 where $u_{x_1} \dots u_{z_6}$ are unknown displacement variables of the problem.

166 2.2 Lagrange expansion models

167 Another class utilizes the Lagrange polynomial as the expansion functions F_τ , named the
168 Lagrange Expansion (LE) model. Within these models, the cross-section can be divided into
169 sub-domains, which are connected with Lagrange Points (LPs). The Lagrange polynomials are
170 usually given in terms of normalized coordinates, and any arbitrary cross-sectional geometry
171 can be described with the help of isoparametric formulation. The simplest quadrilateral
172 Lagrange polynomial is the four-point (L4) set, and the corresponding functions are:

$$F_\tau = \frac{1}{4}(1 + r r_\tau)(1 + s s_\tau), \quad \tau = 1, 2, 3, 4 \tag{4}$$

173 where r and s are the normalized coordinates in the natural reference system, and (r_τ, s_τ) are
174 the coordinates of point τ .

175 Therefore, the 3D displacement of LE model with four-point Lagrange polynomials can
176 be given as:

$$\begin{aligned}
u_x(x, y, z) &= F_1u_{x_1} + F_2u_{x_2} + F_3u_{x_3} + F_4u_{x_4} \\
u_y(x, y, z) &= F_1u_{y_1} + F_2u_{y_2} + F_3u_{y_3} + F_4u_{y_4} \\
u_z(x, y, z) &= F_1u_{z_1} + F_2u_{z_2} + F_3u_{z_3} + F_4u_{z_4}
\end{aligned} \tag{5}$$

177 where $u_{x_1} \dots u_{z_4}$ are unknown variables that are physical translational displacements of each
178 LP.

179 Eq. (5) results from the interpolation of the displacements derived at LPs. Moreover, in
180 practical applications, one can select from quadratic Lagrange polynomials incorporating nine
181 points (L9) or cubic LEs with sixteen points (L16). The physical translational displacements

182 at the LPs within the cross-section correspond to the model's DoFs. Therefore, higher-order
 183 Lagrange polynomials provide enhanced accuracy by offering a more significant number of
 184 DoFs through additional LPs.

185 **2.3 Finite element approach**

186 The FEM is employed to solve for axial displacement vectors as described in Eq. (1). Ac-
 187 cordingly, the displacement field can be rewritten as:

$$\mathbf{u}(x, y, z) = F_\tau(x, z)N_i(y)\mathbf{u}_{\tau i}, \quad i = 1, \dots, N_{NE} \quad (6)$$

188 where N_i denotes the shape function associated with beam node i , $u_{\tau i}$ is the nodal displace-
 189 ment vector, and N_{NE} represents the number of nodes within each beam element. Similarly,
 190 the virtual variation of the displacement can be expressed as:

$$\delta\mathbf{u}(x, y, z) = \delta\mathbf{u}_{sj}F_s(x, z)N_j(y), \quad j = 1, \dots, N_{NE} \quad (7)$$

191 The detailed information on beam shape functions can be found in (Carrera et al., 2014).
 192 Commonly adopted beam elements include two-node linear (B2), three-node quadratic (B3),
 193 and four-node cubic (B4) configurations. Notably, the selection of beam elements is inde-
 194 pendent of the choice of expansion functions, which is a significant flexibility for 1D CUF
 195 models.

196 The 3D strain field, $\boldsymbol{\varepsilon} = \{\varepsilon_{xx}, \varepsilon_{yy}, \varepsilon_{zz}, \varepsilon_{xy}, \varepsilon_{xz}, \varepsilon_{yz}\}^T$, can be obtained through the strain-
 197 displacement relation, which can be expressed in a vectorial notation:

$$\boldsymbol{\varepsilon} = \mathbf{B}\mathbf{u} \quad (8)$$

198 where \mathbf{B} is the linear differential operator with two contributions:

$$\mathbf{B} = \mathbf{B}_\Omega + \mathbf{B}_y = \begin{bmatrix} \frac{\partial}{\partial x} & 0 & 0 \\ 0 & 0 & 0 \\ 0 & 0 & \frac{\partial}{\partial z} \\ 0 & \frac{\partial}{\partial x} & 0 \\ \frac{\partial}{\partial z} & 0 & \frac{\partial}{\partial x} \\ 0 & \frac{\partial}{\partial z} & 0 \end{bmatrix} + \begin{bmatrix} 0 & 0 & 0 \\ 0 & \frac{\partial}{\partial y} & 0 \\ 0 & 0 & 0 \\ \frac{\partial}{\partial y} & 0 & 0 \\ 0 & 0 & 0 \\ 0 & 0 & \frac{\partial}{\partial y} \end{bmatrix} \quad (9)$$

199 The 3D stress field, $\boldsymbol{\sigma} = \{\sigma_{xx}, \sigma_{yy}, \sigma_{zz}, \sigma_{xy}, \sigma_{xz}, \sigma_{yz}\}^T$, can be calculated through the con-
 200 stitutive relation, which is expressed as:

$$\boldsymbol{\sigma} = \mathbf{C}_d \boldsymbol{\varepsilon} \quad (10)$$

201 where \mathbf{C}_d is a 6×6 represents the 6×6 stiffness matrix of the damaged material. This study
 202 addresses material nonlinearities resulting from damage, requiring a Newton–Raphson scheme.
 203 The secant stiffness matrix is used in the incremental process for its simpler implementation
 204 than the tangent stiffness matrix, though this may result in slower convergence. More details
 205 on the damage model will be introduced later.

206 2.4 Component-Wise approach

207 Due to the previously mentioned physical meaning of Lagrange polynomials, the Component-
 208 Wise approach, an extension of 1D-CUF models, has been developed to accurately represent
 209 composite structures made of diverse materials (Nagaraj et al., 2022; Kaleel et al., 2018).
 210 This approach is also effective for RC structures made of steel and concrete. As depicted
 211 in Fig. 1, the cross-section of such structure is discretized into multiple elements according
 212 to the material. Here, steel is denoted by the red elements, while concrete is indicated in
 213 grey. Lagrange points are assigned at their boundaries to maintain displacement continuity
 214 at the interfaces of steel and concrete components. The behavior of RC structures is then
 215 modeled with the LEs over the discretized beam elements. This CW approach allows for the
 216 independent and simultaneous consideration of actual material and geometric properties of
 217 each component, leading to a more accurate representation of the structural behavior.

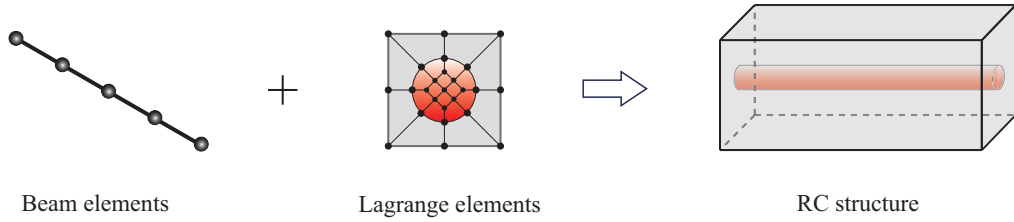


Figure 1: An illustration of the beam model with CW approach for modeling RC structures

3 Node-dependent kinematics approach

According to Section 2, the 3D displacement field of beam elements is first approximated by the cross-sectional expansion $F_\tau(x, z)$ at node i , which is subsequently interpolated along the beam axis using the FE shape functions $N_i(y)$. Typically, uniform cross-sectional expansions are applied across all FE beam nodes. Classical beam theories can be realized in the framework of CUF by designing appropriate cross-sectional expansion. The aforementioned advanced TE and LE can overcome some limitations of these classical theories, particularly in complex scenarios, albeit at an increased computational cost.

In most cases, refined or higher-order models are only required in critical regions of the structure, such as areas with constraints or loadings and zones with concentrated stresses. In contrast, classical or lower-order models are sufficient for the rest of the non-critical regions. This strategy can reduce computational costs under the premise of high accuracy. For the connection between non-critical and critical zones, a node-dependent kinematics approach is proposed for transition. The NDK approach was first introduced in (Carrera and Zappino, 2017) and has since found widespread uses such as (Nagaraj et al., 2023; Scano et al., 2023).

3.1 Beam element with Node-dependent kinematics

An example of a beam structure is illustrated in Fig. 2, where the critical and non-critical regions are denoted by grey and white, respectively. In the NDK framework, the cross-sectional mechanical description $F_\tau(x, z)$ on each node is not uniform anymore, and it is further related to the node i , leading to node-dependent cross-sectional kinematics $F_\tau^i(x, z)$. Consequently, the number of terms in the expansion, M , differs at each node and is replaced with the notation M^i . The displacement fields are smeared through the same FE beam shape functions to ensure displacement continuity across all points. The displacement representation

241 for NDK beam elements, therefore, adopts the following form:

$$\mathbf{u}(x, y, z) = F_\tau^i(x, z)N_i(y)\mathbf{u}_{\tau i}, \quad i = 1, \dots, N_{NE}; \quad \tau = 1, \dots, M^i \quad (11)$$

242 Besides, the variation of the corresponding displacement can be written as:

$$\delta\mathbf{u}(x, y, z) = \delta\mathbf{u}_{sj}F_s^j(x, z)N_j(y), \quad j = 1, \dots, N_{NE}; \quad s = 1, \dots, M^j \quad (12)$$

243 Figure 2 selects a two-node beam element within the transition zone for demonstration.
 244 Assuming the left node, marked in red, adopts a first-order TE while the right node, depicted
 245 in black, utilizes a linear LE with four nodes, the displacement field of Eq. (11) can be
 246 expressed as:

$$\mathbf{u}(x, y, z) = N_1(y)[\mathbf{u}_{11} + \mathbf{u}_{21}x + \mathbf{u}_{31}z] + N_2(y)[\mathbf{u}_{12}L_1 + \mathbf{u}_{22}L_2 + \mathbf{u}_{32}L_3 + \mathbf{u}_{42}L_4] \quad (13)$$

where L_1, \dots, L_4 are Lagrange expression from Eq. (4).

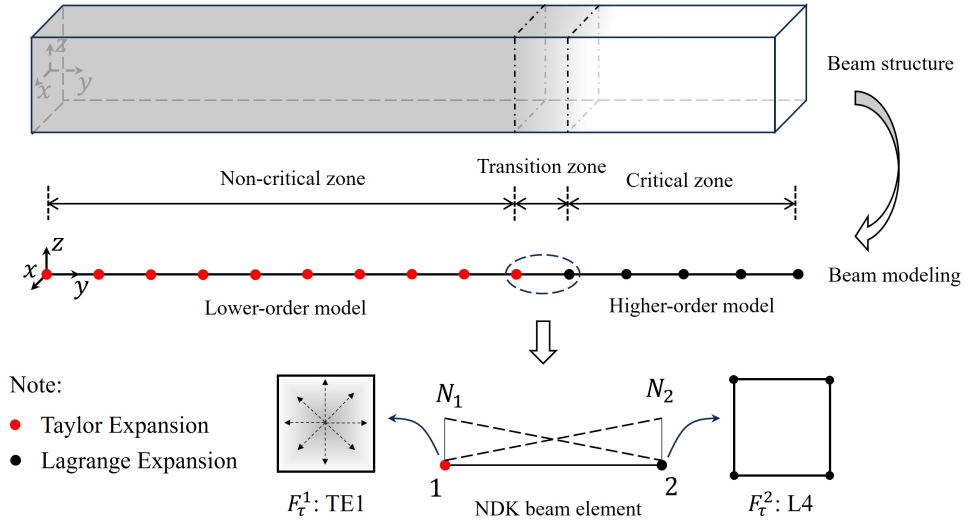


Figure 2: A CUF-based 1D model with NDK approach

247

248 3.2 FE governing equations

249 The governing equation for static problems is derived from the principle of virtual displacements,
 250 which states the equality of the external virtual work (δL_{ext}) and internal virtual work

251 (δL_{int}) . For simplicity, they are expressed as:

$$\delta L_{\text{int}} = \int_V \delta \boldsymbol{\varepsilon}^T \boldsymbol{\sigma} dV = \delta \mathbf{u}_{sj}^T \mathbf{K}^{\tau sij} \mathbf{u}_{\tau i} \quad (14)$$

252

$$\delta L_{\text{ext}} = \int_V \delta \mathbf{u}^T \mathbf{F} dV = \delta \mathbf{u}_{sj}^T \int_V N_j F_s^j \mathbf{F} dV = \delta \mathbf{u}_{sj}^T \mathbf{F}_{sj} \quad (15)$$

253 with

$$\mathbf{K}^{\tau sij} = \int_l \int_{\Omega} [\mathbf{B}^T(N_j(y)F_s^j(x, z))\mathbf{C}_d\mathbf{B}(F_{\tau}^i(x, z)N_i(y))]d\Omega dl \quad (16)$$

254 where $\mathbf{K}^{\tau sij}$ is the fundamental nucleus in the form of 3×3 stiffness matrix; l and Ω represent
 255 the length of beam element and area of cross-section respectively; i, j , and τ, s are indexes
 256 related to beam shape function and cross-sectional expansion function respectively. \mathbf{F} is the
 257 external load and \mathbf{F}_{sj} is the load vector in a 3×1 array. Thus, the governing equation can
 258 be expressed as:

$$\mathbf{K}^{\tau sij} \mathbf{u}_{\tau i} = \mathbf{F}_{sj} \quad (17)$$

259 The matrix $\mathbf{K}^{\tau sij}$ is the basic block from which the stiffness matrix of the whole structure
 260 can be constructed automatically. It can be expressed as:

$$\mathbf{K}^{\tau sij} = \begin{bmatrix} k_{xx}^{\tau sij} & k_{xy}^{\tau sij} & k_{xz}^{\tau sij} \\ k_{yx}^{\tau sij} & k_{yy}^{\tau sij} & k_{yz}^{\tau sij} \\ k_{zx}^{\tau sij} & k_{zy}^{\tau sij} & k_{zz}^{\tau sij} \end{bmatrix} \quad (18)$$

261 Extended forms for each component in Eq. (18) are detailed in (Carrera and Zappino,
 262 2017). For brevity, the explicit expression of the first component $k_{xx}^{\tau sij}$, for an undamaged
 263 isotropic material, is given as follows:

$$k_{xx}^{\tau sij} = C_{22} \int_{\Omega} F_{\tau,x}^i F_{s,x}^j d\Omega \int_l N_i N_j dy + C_{66} \int_{\Omega} F_{\tau,z}^i F_{s,z}^j d\Omega \int_l N_i N_j dy + C_{44} \int_{\Omega} F_{\tau}^i F_s^j d\Omega \int_l N_{i,y} N_{j,y} dy \quad (19)$$

264 where C_{22} , C_{44} , and C_{66} are components of the material stiffness matrix, typically determined
 265 by the material's modulus of elasticity and Poisson's ratio.

4 Modified Mazars damage models

In this section, the isotropic concrete damage model proposed by Mazars (Mazars, 1984) is presented to capture the damage behavior of concrete. The model is modified with the fracture energy regularization technique to alleviate the mesh dependence based on the tensile and compressive constitutive laws (Arruda et al., 2022). The modified Mazars damage model does not consider permanent strains compared to other models. However, it is adequate for the damage analysis of RC structures subjected to quasi-static loads due to the role of steel reinforcement in governing the plastic behavior of such structures. To this end, the Von Mises yield criterion is employed to describe the plasticity of steel reinforcements.

According to (Mazars, 1984), the evolution of isotropic material stiffness is directly controlled by one scalar damage variable d , which ranges from 0 to 1.0. The formulation of the original Mazars damage model is given as follows:

$$\boldsymbol{\sigma} = \mathbf{C}_d \boldsymbol{\varepsilon} = (1 - d) \mathbf{C} \boldsymbol{\varepsilon} \quad (20)$$

where \mathbf{C} represents the material stiffness matrix without damage.

In the Mazars damage model, damage initiation and evolution are governed exclusively by positive strains in the principal directions. Therefore, Mazars introduced an equivalent strain, denoted as ε_{eq} , to cover this behavior. This equivalent strain is calculated according to the following expression:

$$\varepsilon_{eq}(\boldsymbol{\varepsilon}) = \sqrt{\sum_{i=1}^3 \langle \varepsilon_i \rangle_+^2} \quad (21)$$

in which $\langle \cdot \rangle_+$ is the Macauley bracket for picking out the positive value, and ε_i are the principle strains.

Subsequently, the loading function, denoted as $f(\boldsymbol{\varepsilon}, \kappa) = \varepsilon_{eq}(\boldsymbol{\varepsilon}) - \kappa$, depends on the equivalent strain and a damage threshold κ . Before damage occurrence, κ is a material constant that equals the ultimate tensile strain. After damage initiation, it is updated to the current value of ε_{eq} . If $f(\boldsymbol{\varepsilon}, \kappa) = 0$ occurs, it indicates the onset of damage, requiring an update to the damage variable. This update is governed by a linear combination of tensile

290 and compressive damage variables d_t and d_c , and the formulation is expressed as:

$$d = \alpha_t d_t + \alpha_c d_c \quad (22)$$

291 where α_t and α_c are weights factors for the tensile and compressive damage variables, d_t and
 292 compression d_c , respectively. The explicit calculation of α_t and α_c can be found in (Arruda
 293 et al., 2022).

294 Rather than using original damage propagation laws for d_t and d_c from (Mazars, 1984), this
 295 work adopts modified damage evolution laws based on concrete stress-strain relations from
 296 fib Model Code 2010 (MC2010) (fib special activity group, 2013), which are more practical.
 297 Additionally, a fracture energy regularization technique based on the crack band model is
 298 employed to regularize the softening behavior and address the mesh dependency issues.

299 For tensile responses, the bilinear softening constitutive law from MC2010 may lead to
 300 numerical convergence issues when the stress diminishes to zero and the damage ascends to
 301 one. To circumvent this, a classical constitutive law with an exponential softening curve is
 302 employed. The explicit formulation of tensile damage evolution is derived and expressed as:

$$d_t = g_t(\kappa_t) = 1 - \frac{\varepsilon_{d0}}{\kappa_t} \exp\left(\frac{\varepsilon_{d0} - \kappa_t}{\varepsilon_{tu} - \varepsilon_{d0}}\right) \quad (23)$$

303 where ε_{d0} is the threshold elastic strain corresponding to the peak stress, also known as the
 304 mean uniaxial tensile strength f_{ctm} ; ε_{tu} signifies the equivalent ultimate strain for bilinear
 305 softening and is associated with the volumetric fracture energy g_{ft} and crack bandwidth l_c .

306 Similarly, the damage evolution law for compression is derived from the compressive stress-
 307 strain relationship, which can be expressed as follows:

$$d_c = g_c(\kappa_c) = \begin{cases} 1 - \frac{(k \times \eta - \eta^2) f_{cm}}{(1 + (k-2) \times \eta) E_{cm} \kappa_c} & \text{if } \kappa_c \leq \varepsilon_{c1} \\ 1 - \frac{f_{cm}}{E_{cm} \kappa_c} & \text{if } \varepsilon_{c1} < \kappa_c \leq \varepsilon_{c2} \\ 1 + \frac{k_1}{E_{cm}} - \frac{k_2}{E_{cm} \kappa_c} & \text{if } \varepsilon_{c2} < \kappa_c \leq \varepsilon_{cres} \\ 1 - \frac{\sigma_{cres}}{E_{cm} \kappa_c} & \text{if } \varepsilon_{cres} < \kappa_c \end{cases} \quad (24)$$

with

$$\kappa_c = \frac{\kappa_t}{\nu\sqrt{2}}; \quad \eta = \frac{\kappa_c}{\varepsilon_{c1}}; \quad k = \frac{1.05E_{cm}\varepsilon_{c1}}{f_{cm}}; \quad k_1 = \frac{f_{cm}}{(\varepsilon_{cu} - \varepsilon_{c2})}; \quad k_2 = f_{cm} + k_1 \times \varepsilon_{c2};$$

308 where f_{cm} is the mean compressive strength of the concrete; E_{cm} denotes the secant Young's
309 modulus; k , k_1 and k_2 are parameters from (EN, 2005) to describe the softening part of consti-
310 tutive laws; ε_{c1} and ε_{c2} are strain parameters adopted from (EN, 2005); η is a unidimensional
311 strain ratio provided in (fib special activity group, 2013). σ_{cres} is residual compressive stress
312 which ensures stress never reaches 0.0 to avoid convergence issues; ε_{cres} is the corresponding
313 residual compressive strain; ε_{cu} is the equivalent ultimate compressive strain when neglecting
314 the residual stress, and is associated with the compressive volumetric fracture energy g_{fc} and
315 crack bandwidth l_c .

316 One key issue in fracture energy regularization is determining the correct value of l_c for
317 obtaining objective numerical results. It is recognized that various factors, including element
318 shape, element order, and element size, can influence the value of l_c . In this work, the
319 estimation method of l_c from (Shen et al., 2023c) has been adopted. More details of this
320 method can be explored in (Shen et al., 2023c).

321 5 Numerical examples

322 This section presents four illustrative examples of reinforced concrete structures selected from
323 existing literature to demonstrate the proposed approach's numerical performance. The first
324 three examples, which focus on RC beams, are based on experimental campaigns and employ
325 a displacement-control method for the numerical simulations. The last example is a numerical
326 model of an RC frame structure.

327 5.1 Notched reinforced concrete beam under tension

328 The first example is a direct tension test on a notched RC beam, which was conducted
329 experimentally in (Ouyang et al., 1997). Though the CUF-CW solution has been previously

330 applied to this case (Nagaraj and Maiaru, 2023), further investigation is now placed on NDK
 331 models using this simple example. The concrete beam is reinforced with three evenly spaced
 332 longitudinal bars. Two notches, each 10 mm deep and 12.7 mm wide, are prefabricated in the
 333 middle to initiate the first crack. Fig. 3 depicts the overall load layout and geometries. The
 334 left end is fixed in all directions, while a displacement-controlled pressure is applied to the
 335 right end. The material properties are adopted from (Nagaraj and Maiaru, 2023) and listed
 336 in Table 1.

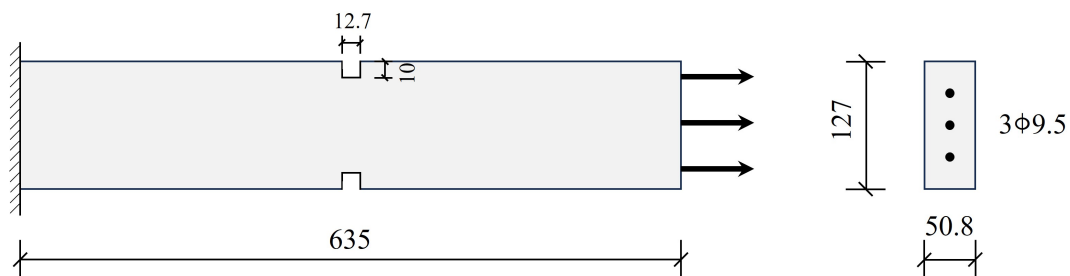


Figure 3: Load layout and geometry of notched RC beams under direct tension (Unit: mm)

Table 1: Material properties of the notched RC beams

Material type	E (GPa)	f_{ctm} (MPa)	f_{cm} (MPa)	G_{ft} (N/m)	G_{fc} (N/m)	ν	f_y (MPa)
Concrete	27.349	3.19	44	144	22150	0.175	-
Steel	191.584	-	-	-	-	0.28	508

337 Beam element discretization is conducted along the longitudinal axis of the structure,
 338 with Fig. 4 (a) illustrating that black dots stand for the nodes of beam elements. More beam
 339 elements are assigned around the middle notches as suggested from (Nagaraj and Maiaru,
 340 2023). This refinement may be critical for accurately capturing the stress concentration and
 341 subsequent damage initiation. Cross-sectional discretizations are visualized in Fig. 4 (b),
 342 where red circles represent the steel component within the beam. The steel is integrated into
 343 the concrete matrix using LPs so that displacement continuity can be satisfied, which is also
 344 the strategy of the CW approach.

345 In (Nagaraj and Maiaru, 2023), only 5 and 7 quadratic beam elements with quadratic
 346 Lagrange elements were employed. Although these models presented satisfactory correlations
 347 with experimental load-displacement curves, the limited number of beam elements constrained
 348 the prediction of accurate damage distribution. The current analysis employs a finer mesh
 349 with 17 quadratic beam elements coupled with the same quadratic Lagrange elements for

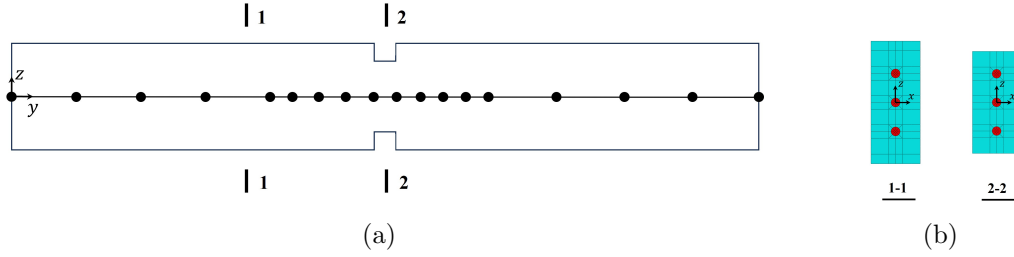


Figure 4: (a) FE discretization of beam elements and (b) cross-sectional discretization for the notched RC beam

cross-sectional expansion. The beam model in which all nodes are expanded via LEs is named the refined CW model, as depicted in Fig. 5 (a). This model can enhance the numerical accuracy, but the required DoFs are relatively high. For the investigation of the NDK approach, two models are presented in Fig. 5 (b) and (c). Notably, both NDK models adopt an identical mesh discretization to the refined CW model. The difference lies in the expansion functions assigned to specific beam nodes as needed. For instance, TEs are utilized for the beam element nodes with cyan in Fig. 5 (b) and (c), and LEs are employed for the remaining nodes. Compared to the NDK1 model, the NDK2 model tries to increase the number of beam nodes using TEs, further reducing computational expenses. Moreover, the influence of TE order on the structural analysis is also investigated in this part. All information of different models is listed in Table 2.

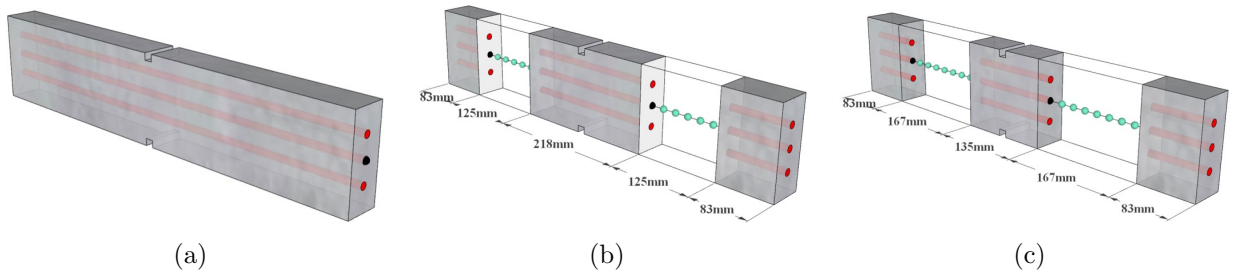


Figure 5: Different models adopted for the analysis of the notched RC beam: (a) Refined CW model; (b) NDK1 model; (c) NDK2 model

Table 2: Model information of the notched RC beams

Model No.	Model 1	Model 2	Model 3	Model 4	Model 5	Model 6	Model 7
Model type	Refined	NDK1	NDK1	NDK1	NDK2	NDK2	NDK2
TE Order	-	TE1	TE2	TE3	TE1	TE2	TE3
DoFs	43,677	31,257	31,347	31,467	26,289	26,415	26,583

Figure 6 presents the load-deflection responses of the notched RC beam according to the

362 models above, alongside the corresponding experimental results for comparison. The curve of
 363 Model 1 agrees well with the experimental data, demonstrating the strong capability of the
 364 CW approach in addressing this type of composite structure. Therefore, Model 1 should be
 365 regarded as a refined CW model whose performance can be considered a benchmark for NDK
 366 models.

367 When the NDK approach is applied, as illustrated in Figures 6, all NDK models initially
 368 exhibit linear behavior identical to that of Model 1. Upon the onset of damage, all NDK
 369 models present a consistent structural response. However, the hardening curves of all NDK
 370 models are marginally higher than those observed in the experimental data and simulated by
 371 Model 1. This slight discrepancy may be attributed to the reduced DoFs in some beam areas.
 372 Comparison between Fig. 6 (a) and (b) reveals that the NDK2 model predicts marginally
 373 steeper hardening curves, suggesting that the reduction in DoFs has a slight impact on the
 374 structural response during hardening.

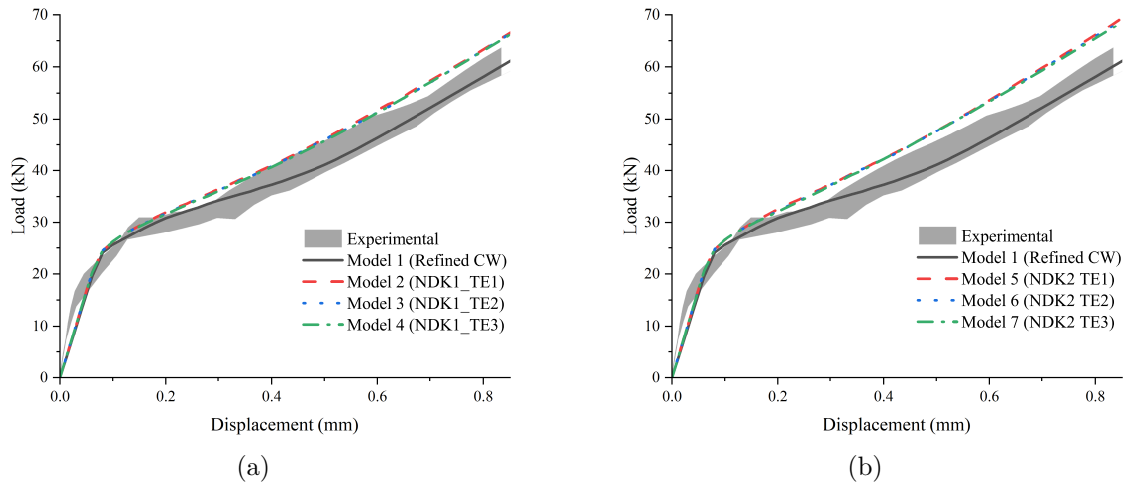


Figure 6: Load-deflection curves from experimental test, refined CW model, (a) NDK1 models, and (b) NDK2 models for the notched RC beam

375 To better understand the previously described discrepancy, Fig. 7 presents the final dam-
 376 age distribution for each model. According to Fig. 7 (a), the expected pattern is observed:
 377 The entire beam exhibits damage to varying degrees, with a fully damaged zone appearing
 378 distinctly and periodically along the beam. The concrete between these zones shows signs
 379 of unloading, indicating strain increments are localized in some narrow bands while the rest
 380 undergo unloading.

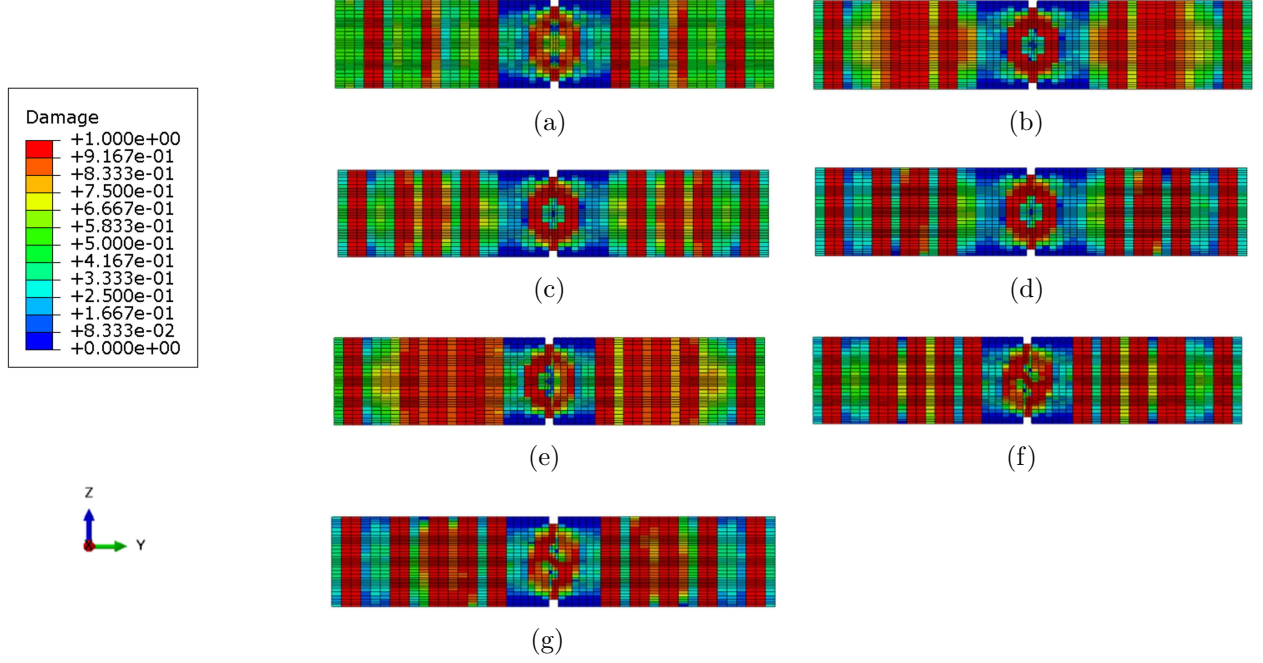


Figure 7: Final damage distributions of the notched RC beam from: (a) Model 1 (Refined CW); (b) Model 2 (NDK1 TE1); (c) Model 3 (NDK1 TE2); (d) Model 4 (NDK1 TE3); (e) Model 5 (NDK2 TE1); (f) Model 6 (NDK2 TE2); (g) Model 7 (NDK2 TE3)

381 In contrast, Fig. 7 (b) indicates that areas using linear TE are depicted as fully damaged,
 382 which may not be reasonable. Applying second-order and third-order TEs to the same areas
 383 results in a recurrence of the distributed damage zones, as shown in Figs. 7 (c) and (d), but
 384 they are denser than those in Fig. 7 (a). This phenomenon is also observable from Figs. 7
 385 (e) to g.

386 Therefore, it can be inferred that the NDK models tend to overestimate damage compared
 387 to the refined CW model due to the limited DoFs, which further leads to a relatively higher
 388 hardening structural behavior. The NDK2 models amplify this phenomenon compared to the
 389 NDK1 models due to the increased number of beam elements using TE, which can account
 390 for the slightly higher hardening curves observed in Fig. 7 (b) relative to those from NDK1
 391 models in Fig. 7 (a). Nonetheless, the divergence between the results from NDK models and
 392 experimental data or refined CW model is considered acceptable given the computational
 393 efficiency benefits. Specifically, the NDK2 model demonstrates an approximate 40% reduction
 394 in DoFs compared to the refined CW model, rendering them preferable to the NDK1 model,
 395 which offers about 28.4% reduction in DoFs.

5.2 Four-point bending reinforced concrete beam

RC beams under a four-point bending test are commonly seen in experimental campaigns because they reflect typical working conditions of RC beams. A benchmark experiment, as reported in (Firmo et al., 2018), was simulated using a CUF-based higher-order beam model detailed in (Shen et al., 2023a). Although this model in (Shen et al., 2023a) produced mesh-independent results, it still required a relatively large number of DoFs. Therefore, this study reviews the same benchmark. Fig. 8 shows the load layout and geometric details. The concrete beam is reinforced with stirrups every 60 mm throughout the length. A displacement control method with a maximum value of 25 mm is employed for numerical simulations. The material properties are listed in Table. 3.

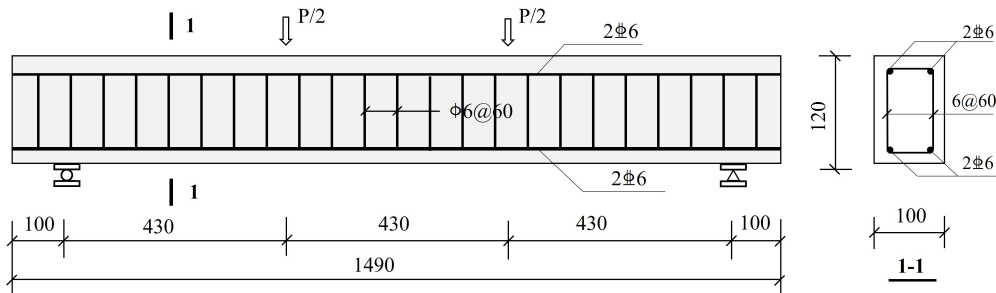


Figure 8: Load layout and geometry of RC beams under four-point bending (Unit: mm)

Table 3: Material properties of the four-point bending RC beam

Material	E (GPa)	f_{ctm} (MPa)	f_{cm} (MPa)	G_{ft} (N/m)	G_{fc} (N/m)	ν	f_y (MPa)	f_{yu} (MPa)
Concrete	31.0	2.8	37	140.0	21000	0.2	-	-
Steel	193	-	-	-	-	0.3	546	691

A half-structure model, as depicted in Fig. 9, was utilized for numerical simulation owing to the symmetry. The nodes on the mid-span symmetry plane were restrained against displacement along the axial coordinate. Fig. 9 (a) illustrates the discretization of beam elements, with black dots representing nodes of beam elements. It should be noted that the node positions and quantities are only for illustration rather than for actual numerical calculation. Fig. 9 (b) presents four cross-sectional discretizations, with gray areas representing the elastic plates for loading and support and the red regions denoting steel components. Nodes at the steel-concrete interface are shared to ensure displacement continuity between steel and concrete components.

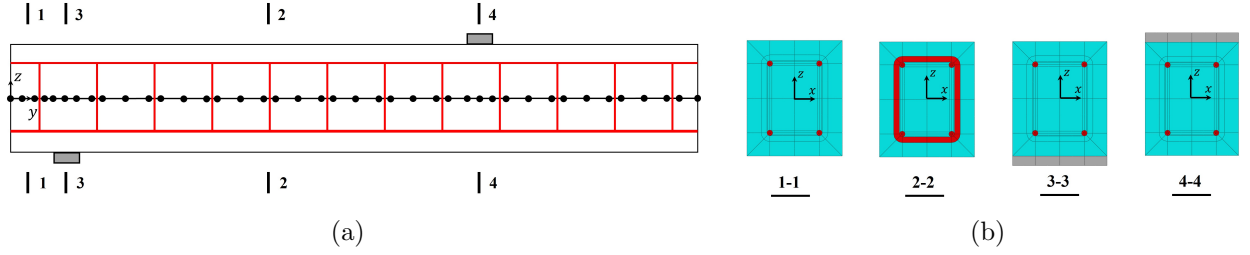


Figure 9: (a) FE discretization of beam elements and (b) cross-sectional discretization for the four-point bending RC beam

415 To evaluate the efficiency of the NDK solution, Table 4 lists six models where model 1
 416 and model 5 employ LEs for all beam nodes, and the rest adopts the NDK approach. Model
 417 1 and model 5 are acknowledged as refined CW solutions because their accuracies have been
 418 confirmed in (Shen et al., 2023a).

Table 4: Model information of the four-point bending RC beam

Model No.	Model 1	Model 2	Model 3	Model 4	Model 5	Model 6
Model type	Refined CW	NDK1	NDK2	NDK3	Refined CW	NDK1
Beam elements	40B2	40B2	40B2	40B2	40B4	40B4
DoFs	55,551	19,263	4,491	4,848	163,743	59,163

419 Based on the refined CW model, three different NDK models are introduced in Fig. 10,
 420 where black nodes are associated with LEs, cyan nodes correspond to TE1, and red nodes
 421 indicate TE3. Since the mid-span of bending RC beams is susceptible to damage and failure,
 422 NDK1 employs LEs in the mid-span and support zones, while the remaining uses TE1. This
 423 strategy ensures detailed damage capture in the critical mid-span region while optimizing
 424 computational resources elsewhere. For comparison, NDK2 and NDK3 apply a greedy ap-
 425 proach in which only the supporting and loading parts are assigned with LEs and employ
 426 TEs elsewhere to highlight the importance of mid-span. It should be noted that all models
 427 adhere to the same cross-sectional discretizations as depicted in Fig. 9 (b).

428 Figure 11 plots the load-deflection response of various models, including the experimental
 429 curve for comparison. Initially, there is an excellent agreement between the experimental data
 430 and the numerical predictions across all models during the elastic phase. The variance between
 431 the numerical and experimental crack loads has been previously discussed in (Shen et al.,
 432 2023a). After the elastic step, Models 3 and 4 start to diverge from the expected behavior,

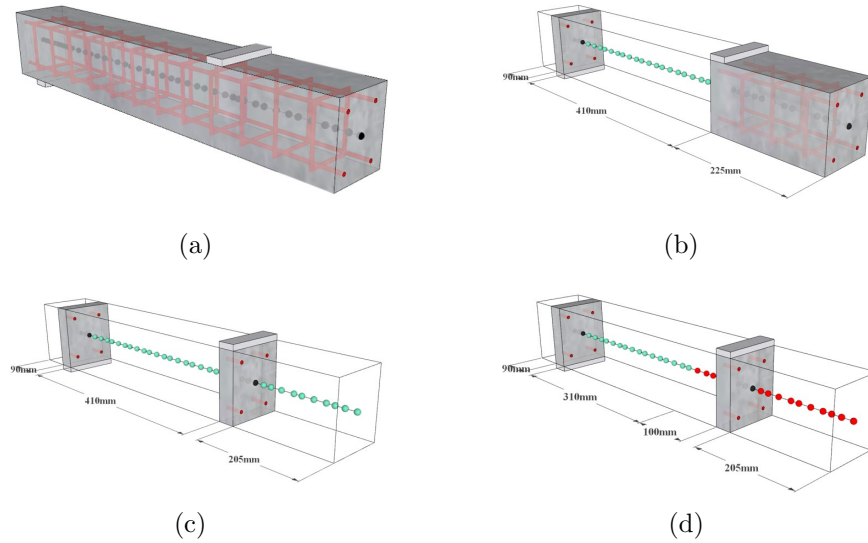


Figure 10: Different models adopted for the analysis of the four-point bending RC beam: (a) Refined CW model; (b) NDK1; (c) NDK2; (d) NDK3. (Cyan stands for TE1 and red represents TE3)

433 failing to simulate the structural response, particularly after steel yielding accurately. The
 434 reason can be found in Figs. 10 (c) and (d), where both models exhibit unreasonable damage
 435 compared to Model 1. This inaccuracy results from the inability of TE to provide sufficient
 436 DoFs despite the significant reduction in computational demands provided by Models 3 and
 437 4. Consequently, while NDK2 and NDK3 models are applicable for the elastic range, they
 438 are too rough to model the correct hardening behavior.

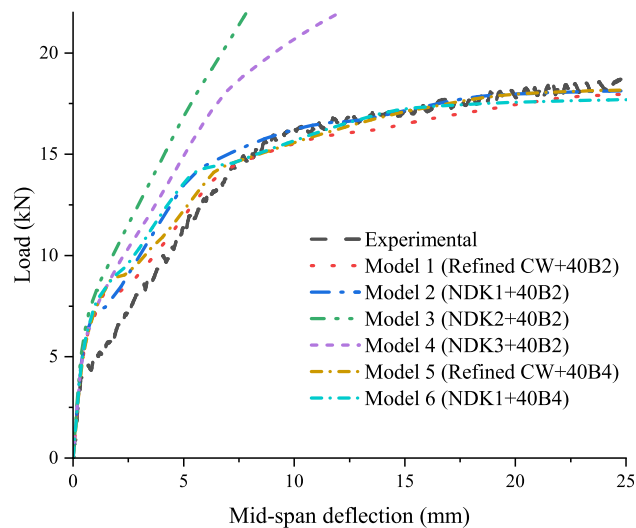


Figure 11: Load-deflection curves for four-point bending RC beams

439 When comparing the responses from Model 1 and Model 2, as depicted in Fig. 11, the
 440 load-deflection curve for the NDK1 model is marginally higher than that of the refined CW

441 model. This variation can be attributed to the reduced DoFs caused by the employment of
 442 TE in the shear regions in Model 2, resulting in a stiffer response. As illustrated in Fig.
 443 12, the damage distribution of Model 2 in the shear area is akin to that of Models 3 and
 444 4. However, the damage captured in the mid-span of Model 2 is similar to that of Model
 445 1. Both models capture vertical damage in the tensile zones and compressive damage at the
 446 top in the mid-span, which agrees with the experimental crack distribution shown in Fig.
 447 13. Hence, Model 2 can still accurately reflect the load-deflection response, highlighting the
 448 greater significance of the structural behavior at the mid-span compared to the shear regions
 449 in this structure. A similar observation on load-displacement curves and damage distributions
 450 is noted when comparing Models 5 and 6, reinforcing the accuracy of the NDK1 model.

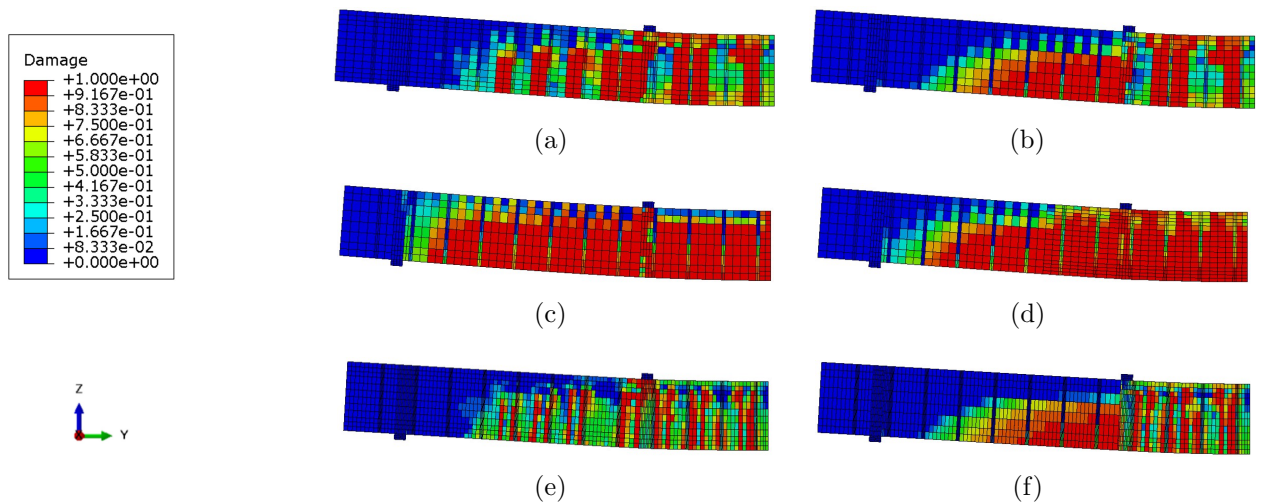


Figure 12: Final damage distribution of four-point bending RC beams from: (a) Model 1 (Refined CW+40B2); (b) Model 2 (NDK1+40B2); (c) Model 3 (NDK2+40B2); (d) Model 4 (NDK3+40B2); (e) Model 5 (Refined CW+40B4); (f) Model 6 (NDK1+40B4)

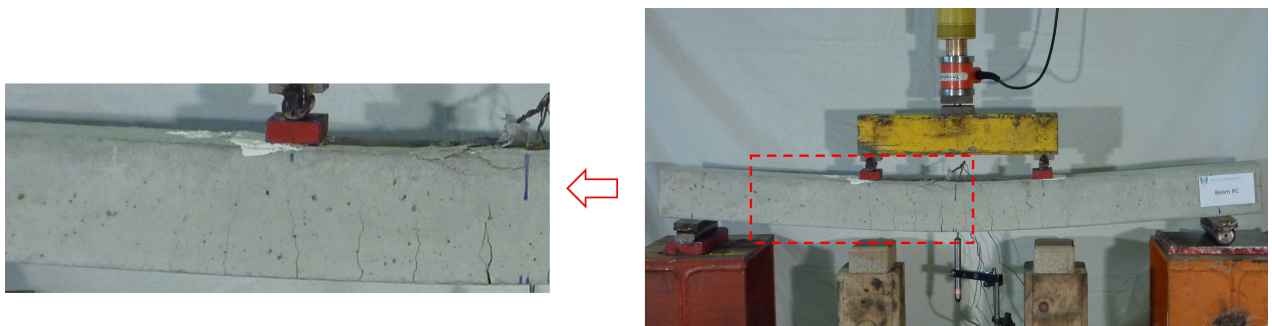


Figure 13: Experimental cracks of four-point bending RC beam (Firmo, 2015)

451 Additionally, the Von Mises stress distributions of concrete and steel for Models 5 and
 452 6 at the final step are depicted in Fig. 14 and Fig. 15, respectively. The Von Mises stress

453 distributions in the middle span of both models are similar. The Von Mises stresses of
 454 concrete in the tensile zones are nearly zero, resulting from tensile strain softening or unloading
 455 due to tensile damage. Meanwhile, the Von Mises stresses in the compressive zones reach
 456 or approximate the compressive strength, indicating the occurrence of compressive damage.
 457 Furthermore, both models demonstrate that the Von Mises stresses in the longitudinal rebars
 458 of the bottom layer reach yield stress, as illustrated in Fig. 15. A discrepancy in the stress
 459 within the shear zones between the two models can be attributed to the limited DoFs in
 460 the shear zones of the NDK models. However, this limitation does not affect the structural
 461 performance of the NDK1 model because the investigated RC beam is flexure-dominant, with
 462 the mid-span being particularly critical and susceptible to damage. NDK1 model employs
 463 higher-order models for the mid-span zone, ensuring its accuracy.

464 Regarding computational costs, Model 2 exhibits an approximately 65% reduction in DoFs
 465 compared to Model 1, while Model 6 offers a similar reduction relative to Model 5. These
 466 findings underscore the advantage of the NDK1 model in balancing computational efficiency
 467 with high fidelity in structural response simulation.

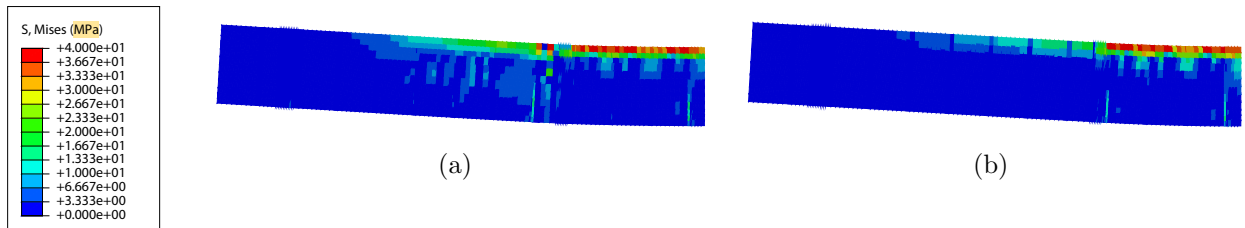


Figure 14: Von Mises stress distribution of concrete in four-point bending RC beam from: (a) Model 5 (Refined CW+40B4); (b) Model 6 (NDK1+40B4) at displacement of 25mm

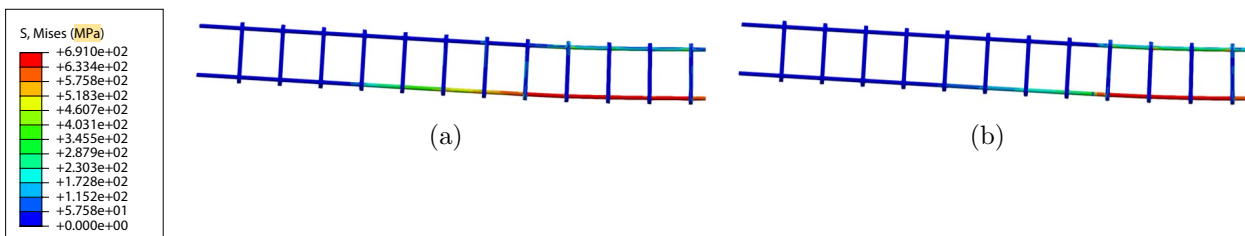


Figure 15: Von Mises stress distribution of steel reinforcement in four-point bending RC beam from: (a) Model 5 (Refined CW+40B4); (b) Model 6 (NDK1+40B4) at displacement of 25mm

468 5.3 Reinforced concrete beam with web openings

469 RC beams with web openings are commonly implemented where passing ducts to accommo-
470 date vital utilities are necessary. These openings inevitably result in a decrease in stiffness
471 and localized damage, weakening the overall structural performance. A detailed investigation
472 of web openings and their surroundings is important. For this reason, an RC beam with web
473 openings, ideal for applying the NDK approach, is examined as the third case study. A group
474 of experimental campaigns for RC beam with web opening was reported in (Elsanadedy et al.,
475 2019). One selected specimen from (Elsanadedy et al., 2019) is illustrated in Fig. 16, where
476 two rectangular web openings with $450 \text{ mm} \times 225 \text{ mm}$ are created in the shear zone of the RC
477 beam. The experiment was specifically designed to investigate the response of an RC beam
478 after introducing post-construction openings without any additional strengthening methods.
479 The rest of the experimental conditions are the same as those from the second case. Accord-
480 ing to (Elsanadedy et al., 2019), the compressive strength of concrete was 50 MPa, measured
481 from cube tests. A strength of 40 MPa is estimated from (fib special activity group, 2013) to
482 align this with cylinder test results. The concrete Young's modulus was unknown; however,
483 preliminary numerical analysis were conducted to approximate the modulus by fitting the
484 experimental linear response. As a result, the concrete's Young's modulus is estimated at 24
485 GPa. Additional material properties are listed in Table 5.

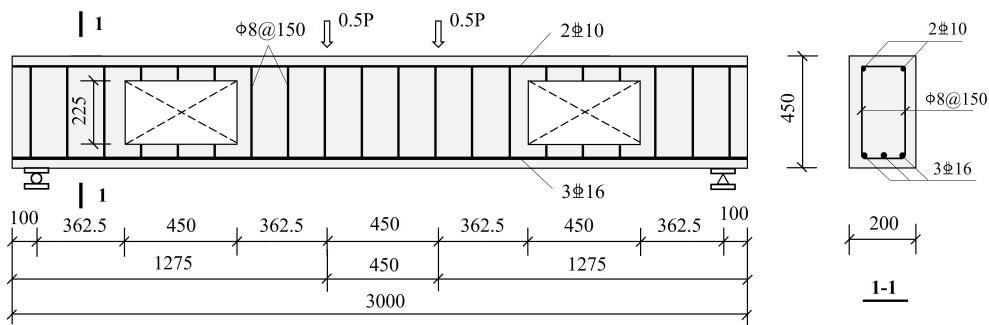


Figure 16: Load layout and geometry of the RC beam with web openings (Unit:mm)

Table 5: Material properties of the RC beam with web openings

Material	E (GPa)	f_{ctm} (MPa)	f_{cm} (MPa)	G_{ft} (N/m)	G_{fc} (N/m)	ν	f_y (MPa)
Concrete	24.0	2.3	40	70.0	21627	0.2	-
Steel	200	-	-	-	-	0.3	575

486 Similarly, only half-structures are modeled for numerical analysis due to the benefit of
 487 symmetry. Fig. 17 (a) illustrates the assignment of beam elements, with six distinct cross-
 488 sections identified to accommodate stirrups, loading plates, and web openings. Fig. 17 (b)
 489 depicts the respective cross-sectional discretizations.

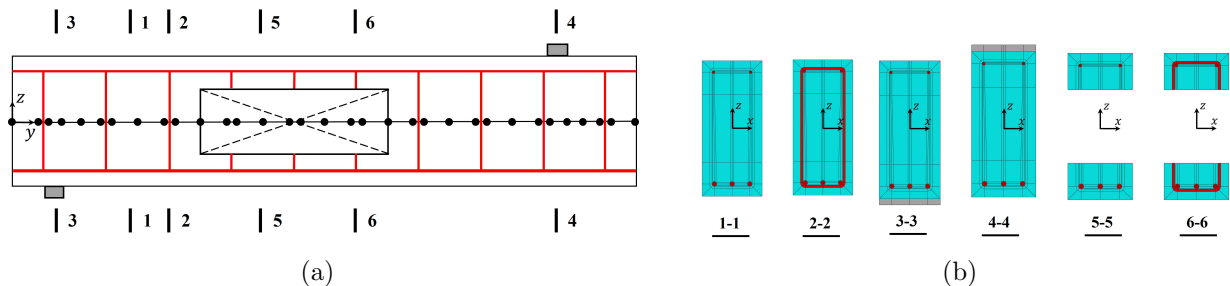


Figure 17: (a) FE discretization of beam elements and (b) cross-sectional discretization for the RC beam with web openings

490 Four numerical models are designed for the damage analysis, and the corresponding model
 491 information is detailed in Table 6. All models employ consistent cross-sectional discretizations
 492 and utilize L9 elements when implementing LEs. Model 1 and Model 2 adopt more beam
 493 elements than Model 3 and Model 4, ensuring sufficient DoFs for simulations. It is expected
 494 that most damage will manifest near the web openings, and some will occur at the bottom
 495 of the midspan. Then, one designed NDK model illustrated in Fig. 18 (b) is applied to
 496 Models 2 and 4 to demonstrate the effectiveness of the NDK approach. From the previous
 497 two examples, the order of TE plays a less important role compared to the length of TE.
 498 Therefore, only linear TE is employed where necessary in Models 2 and 4.

Table 6: Model information of the RC beam with web openings

Model No.	Model 1	Model 2	Model 3	Model 4
Model type	Refined CW	NDK	Refined CW	NDK
Beam order	79B2	79B2	42B4	42B4
DoFs	145,641	94,215	231,558	146,820

499 The load-midspan displacement curves are shown in Fig. 19, comparing numerical sim-
 500 ulations and experimental data. Up to a displacement of 3 mm, numerical results closely
 501 agree with the experimental data, effectively capturing the linear behavior and initial damage
 502 stage. As displacement increases, numerical curves start to deviate from the experimental
 503 benchmark. Despite this divergence, the hardening parts of the numerical curves are still

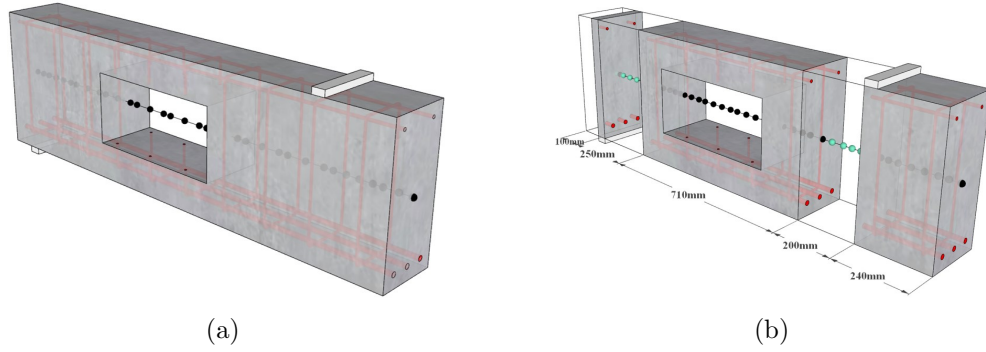


Figure 18: (a) Refined CW model and (b) NDK model for the analysis of the RC beam with web openings

504 parallel to the experimental hardening curves. The experimental curve then reaches the peak
 505 load and exhibits a sharp drop, whereas the numerical curves do not display a significant
 506 decrease. This discrepancy will be explained in the subsequent discussion.

507 When comparing Model 1 to Model 3, their curves coincide closely until reaching the peak
 508 load. The fluctuation in peak loads between these two models is likely due to the difference in
 509 employed element approximation, with cubic beam elements providing better precision over
 510 linear ones. A similar phenomenon is observed between Model 2 and Model 4. Variations
 511 in the results between refined CW models and NDK models are within acceptable ranges
 512 because of the utilization of lower-order TE at some beam element nodes, leading to slightly
 513 softer numerical models. Nevertheless, the NDK model achieves a significant reduction in the
 514 DoFs, approximately 35.3% for B2 elements and 36.6% for B4 elements,

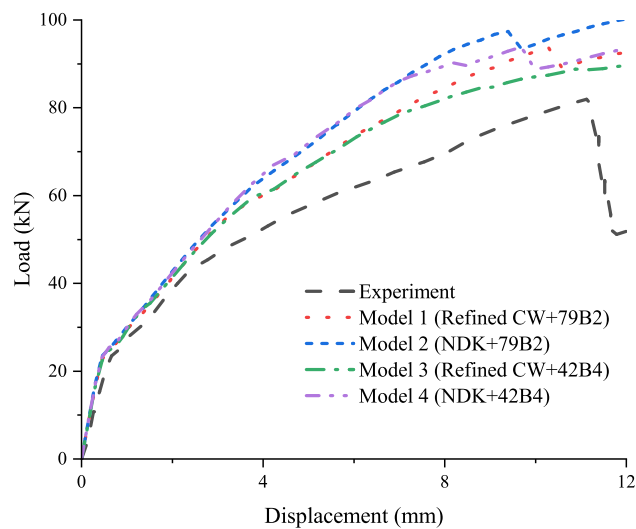


Figure 19: Load-displacement curves for RC beam with web openings

515 The experimental campaign revealed shear failures in the top and bottom chords, as

516 depicted in Fig. 20, which can explain the sharp drop in reaction load observed in the
517 experimental results shown in Fig. 19. This phenomenon can be attributed to the use of
518 U-shaped stirrups, which reduced bonding effectiveness and caused the concrete in the top
519 and bottom chords to behave similarly to plain concrete, thereby leading to the pronounced
520 diagonal shear cracks observed during the experiment.

521 However, the numerical damage patterns shown in Fig. 21 fail to replicate these distinct
522 diagonal cracks, which further explains why the numerical models do not exhibit a similar
523 drop in reaction load as observed in the experimental results in Fig. 19. There are two
524 primary reasons for this discrepancy. Firstly, the assumption of a perfect bond between
525 rebars and surrounding concrete in the proposed numerical models allows the stirrups in the
526 chords to continue resisting shear forces, resulting in vertical damage distributions in the
527 opening zones. Secondly, the damage model used in this work only considers Mode 1 failure,
528 making it difficult to capture Mode 2 shear failure accurately.

529 Although the experimental study detailed in (Elsanadedy et al., 2019) did not report
530 midspan cracks, the numerical models show some damage at the midspan. This discrepancy
531 may be attributed to the damage criterion of the Mazars damage model, which is governed
532 by positive tensile strain and is, therefore, sensitive to tensile damage at the bottom of the
533 midspan. Moreover, some oblique damage distributions are observed close to the opening
534 zones in Fig. 21, which resemble the oblique cracks observed in the same positions in the
535 experimental beam shown in Fig. 20.

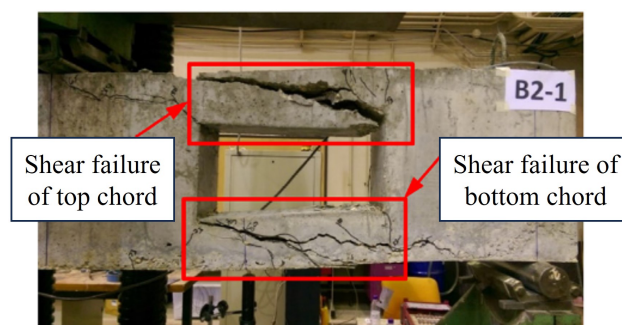


Figure 20: Failures observed from experiments (Elsanadedy et al., 2019)

536 Implementing the NDK approach results in slight variances in damage distributions for
537 NDK models compared to refined CW models, as shown in Fig. 21. Considering that the
538 web openings are large relative to the whole length of the beam, the damage is evident across

539 most beam regions. Thus, the potential for model improvement is limited, and the employed
 540 NDK model likely represents the optimal approach for capturing the damage distribution of
 541 this beam.

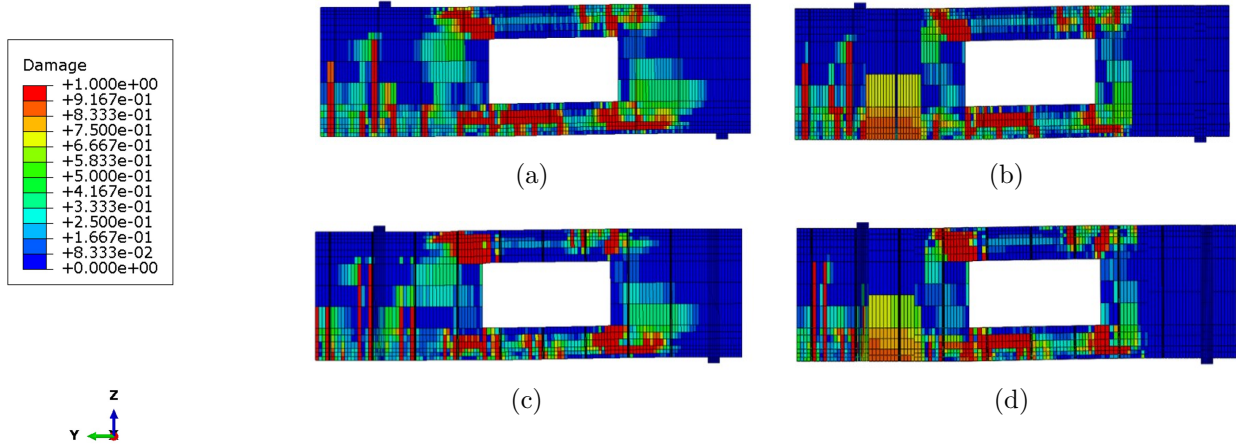


Figure 21: Damage distributions of the RC beam with web openings from: (a) Model 1 (Refined CW+79B2); (b) Model 2 (NDK+79B2); (c) Model 3 (Refined CW+42B4); (d) Model 4 (NDK+42B4) at the displacement of 11 mm

542 5.4 Reinforced concrete frame

543 The last example involves a full-scale RC frame to assess the capability of the proposed
 544 approach in practical engineering scenarios. The experimental campaign, reported in (Baghi
 545 et al., 2018), consisted of three loading phases designed to explore the influence of infill wall
 546 on the behavior of RC frame subjected to a column failure. The initial phase involved elastic
 547 loading of the RC frame without infill walls, followed by a second phase where the frame
 548 infilled with brick walls was loaded until the failure of brick walls. This study specifically
 549 considers the third phase, where the infilled wall was removed, and the bare frame was loaded
 550 until failure. The RC frame was designed to have strong columns and weak beams according
 551 to (EN, 2005). Since the frame was overdesigned and no plastic strains were observed in the
 552 longitudinal reinforcement during the first two loading phases, it was assumed to be as new
 553 before the third loading phase. The height and width of this frame are around 2.55 m and 5 m,
 554 respectively. Fig. 22 depicts the geometry and reinforcement details. A displacement-control
 555 method with a maximum value of 150 mm is employed. The material properties are listed in
 556 Table. 7.

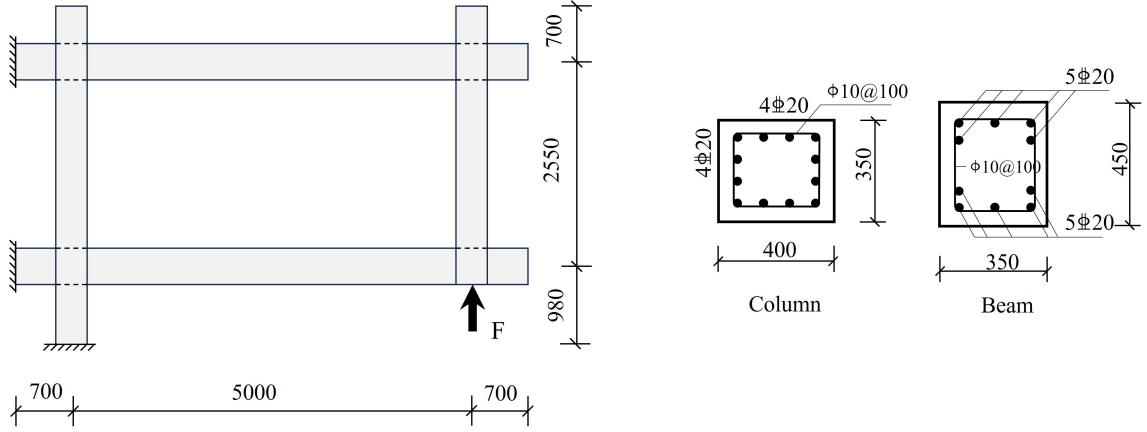


Figure 22: Load layout and geometry of the studied RC frame (Unit: mm)

Table 7: Material properties of the RC frame

Material	E (GPa)	f_{ctm} (MPa)	f_{cm} (MPa)	G_{ft} (N/m)	G_{fc} (N/m)	ν	f_y (MPa)	f_{yu} (MPa)
Concrete	36.858	2.7	43	144.0	22000	0.2	-	-
Steel	200	-	-	-	-	0.3	618	720

557 The structural discretization is detailed in Fig. 23, where beam elements extend along the
558 beam and columns. The black nodes indicating beam element nodes in Fig. 23 (a) are only
559 for illustrative purposes and do not represent their precise locations for calculation. The steel
560 reinforcement within the concrete has been simplified into a square profile while maintaining
561 the same cross-sectional area as its original circular form. This modification not only simplifies
562 the process of cross-sectional discretization but also reduces computational demands. Four
563 distinct cross-sectional discretizations are depicted in Fig. 23 (b) to account for the inclusion
564 of stirrups and the longitudinal rebars from the beam extending into the column. In Fig.
565 23 (b), the steel is highlighted in red, and the surrounding concrete is designated in cyan.
566 The discretization on the beam cross-section is designed based on the assignment of beam
567 elements along the column, enabling node sharing at the beam-column junction. This design
568 can ensure the displacement continuity at the beam-column connection, especially accounting
569 for the horizontal extension of steel rebars from the beam into the column.

570 In total, 416 beam elements are required for the entire structure since the periodic place-
571 ment of stirrups. Four models, detailed in Table 8, are investigated with identical discretiza-
572 tions. However, Model 3 and Model 4 employ quadratic beam elements, and Model 1 and
573 Model 2 adopt linear beam elements. Model 2 and Model 4 apply the NDK approach as de-
574 picted in Fig. 24 (b). LEs are mainly used for nodes at beam-column connections, and nodes

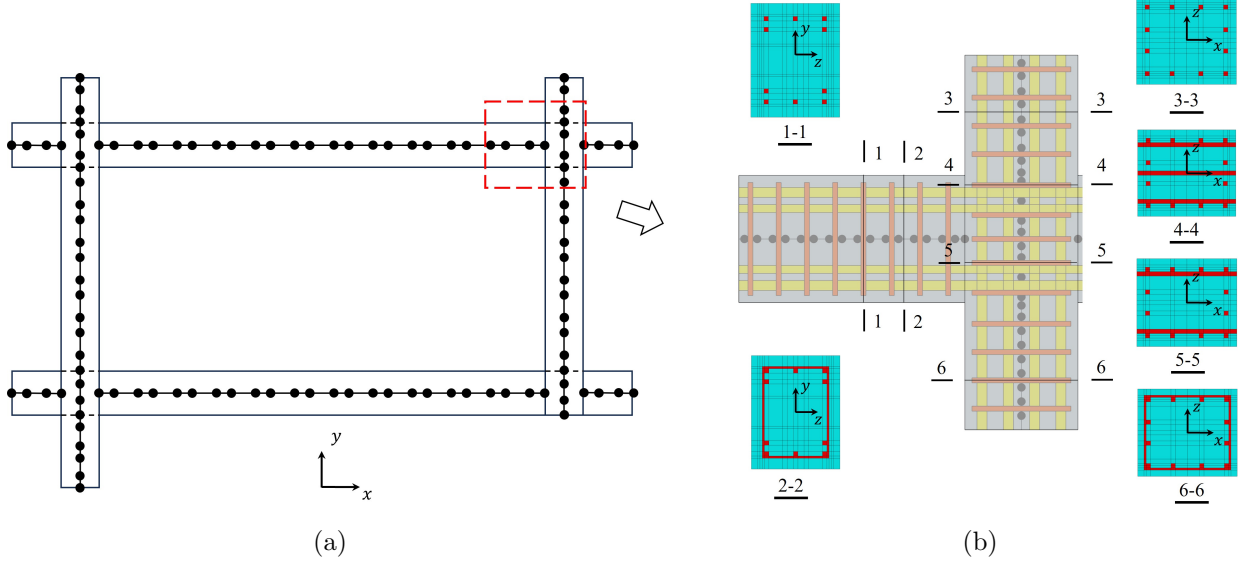


Figure 23: (a) FE discretization of beam elements and (b) cross-sectional discretization for the RC frame

575 in the remaining middle sections are defined using linear TE. Moreover, an ABAQUS model
 576 is also considered for comparison in which C3D8 solid elements are employed for concrete,
 577 and B31 beam elements are adopted for steel. The approximate element size is 40 mm, and
 578 200,598 DOFs are required for this ABAQUS model. Meanwhile, the same modified Mazars
 579 damage model is implemented for the ABAQUS model through the UMAT subroutine.

Table 8: Model information of the RC frame

Model No.	Model 1	Model 2	Model 3	Model 4
Model type	Refined CW	NDK	Refined CW	NDK
Beam order	Linear(B2)	Linear(B2)	Quadratic(B3)	Quadratic(B3)
DoFs	328,968	189,684	1,029,240	545,076

580 The load-deflection diagrams of this RC frame from different numerical models are pre-
 581 sented in Fig. 25, in which experimental and numerical results from (Baghi et al., 2018) are
 582 included for comparison. All numerical models exhibit apparent deviations in initial stiffness
 583 compared to experimental results. However, all numerical models show similar initial stiff-
 584 ness. The discrepancy may be attributed to the formulation of microcracks at the top and
 585 bottom beams when the frame was tested in the first phase (Baghi et al., 2018).

586 Subsequently, the models using modified Mazars damage models in this work, including
 587 CUF models and the ABAQUS model, show slight divergences in the crack load compared to

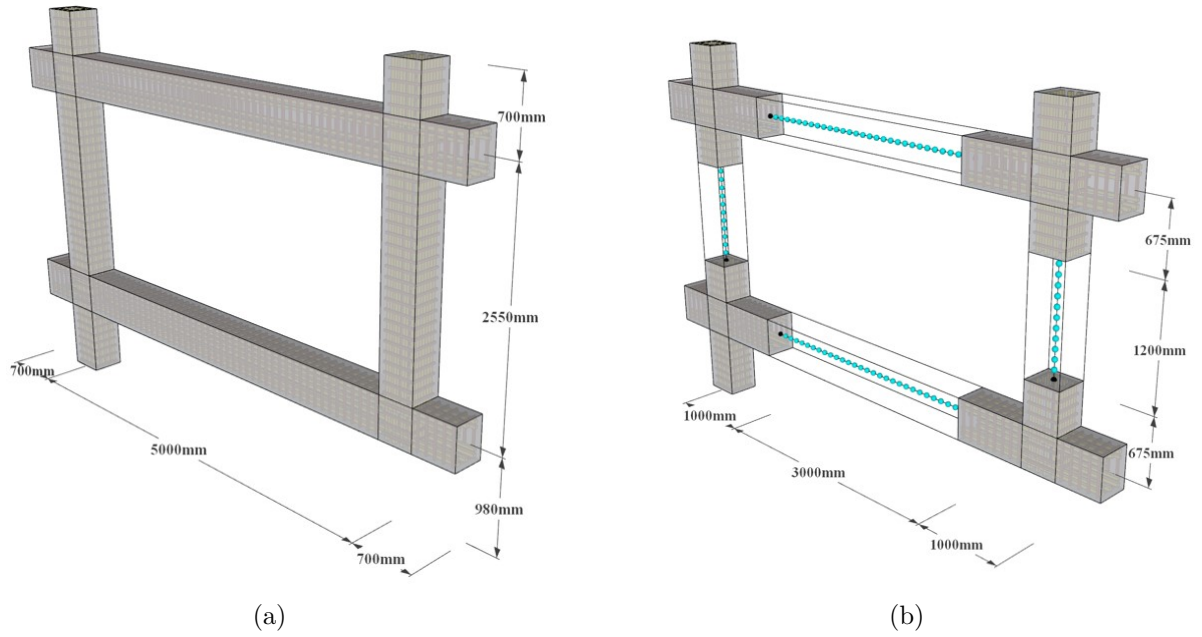


Figure 24: (a) Refined CW model and (b) NDK model for the analysis of the RC frame

588 the OpenSees model from (Baghi et al., 2018), which can be attributed to the use of different
 589 models. Afterward, all numerical models gradually match the experimental results around
 590 the period of steel yielding, when the structural stiffness is further reduced, and the load-
 591 displacement curve begins to flatten. In general, the proximity of the CUF models to the
 592 ABAQUS and OpenSees models throughout the entire loading process and their alignment
 593 with the experimental results in the latter part of the loading process indicates their accuracy.

594 Minor discrepancies are also observed among different CUF models in Fig. 25. Model 1
 595 and Model 2, which employ the linear beam elements, demonstrate slightly lower curves than
 596 Model 3 and Model 4, which adopt the quadratic beam elements. These slight deviations can
 597 be attributed to the fact that the characteristic element length might be underestimated for
 598 quadratic beam elements, as reported in (Shen et al., 2023c), thus leading to a slightly higher
 599 dissipated fracture energy than linear beam elements. Although this sensitivity to element
 600 order presents a challenge, the dependency on mesh size can be mitigated through the method
 601 from (Shen et al., 2023c). Moreover, Model 2 and Model 4 show marginally higher curves
 602 than Model 1 and Model 3, respectively. These observations are consistent with the findings
 603 from prior examples due to the lower-order kinematics employed in NDK models.

604 It was reported that the experimental failure of this bare frame was governed by the
 605 formation of plastic hinges from (Baghi et al., 2018), allowing for plastic rotation of beams

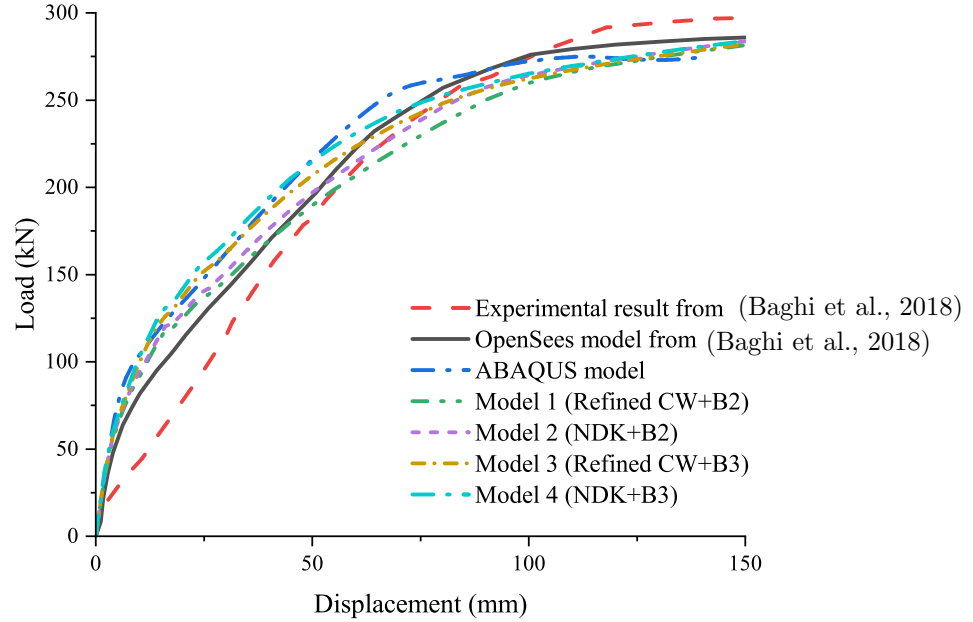


Figure 25: Load-displacement curves for the RC frame

606 at these critical connection points. Fig 26 depicts the deformation and damage distribution
 607 patterns of four CUF models subjected to a displacement of 140 mm, demonstrating similar
 608 plastic rotation of beams along their ends.

609 As experimental cracks were not documented in (Baghi et al., 2018), the corresponding
 610 damage distribution of the ABAQUS model, depicted as Fig. 26 (e), is presented as a ref-
 611 erence. Damage in beams from Model 1 and Model 2 is continuous and uniform, whereas
 612 the ABAQUS model exhibits periodically spaced strip damage. This discrepancy arises from
 613 differences in element size between the models. The beam element length in the CUF models
 614 for unconfined concrete is approximately 100 mm, while the element size in the ABAQUS
 615 model is around 40 mm. Models 3 and 4 with quadratic beam elements display strip damage
 616 distributions in the beams similar to those observed in the ABAQUS model. The distinction
 617 between Models 1 and 3 is attributed to the different orders of beam elements. In continuum
 618 damage models, strain-softening behavior resulting from damage tends to be uniform across
 619 the entire linear beam element. In contrast, only part of the quadratic beam element under-
 620 goes strain-softening, while the remainder experiences unloading, as reported in (Jirásek and
 621 Bauer, 2012).

622 A minor discrepancy in damage distribution in the middle span of beams between Mod-
 623 els 3 and 4 can be observed, attributed to the use of different expansion functions. This

624 phenomenon has similarly been reported in previous comparisons between refined CW and
 625 NDK models. Overall, the damage distributions of CUF models align with those from the
 626 ABAQUS model, enhancing the accuracy of the proposed method in this work.

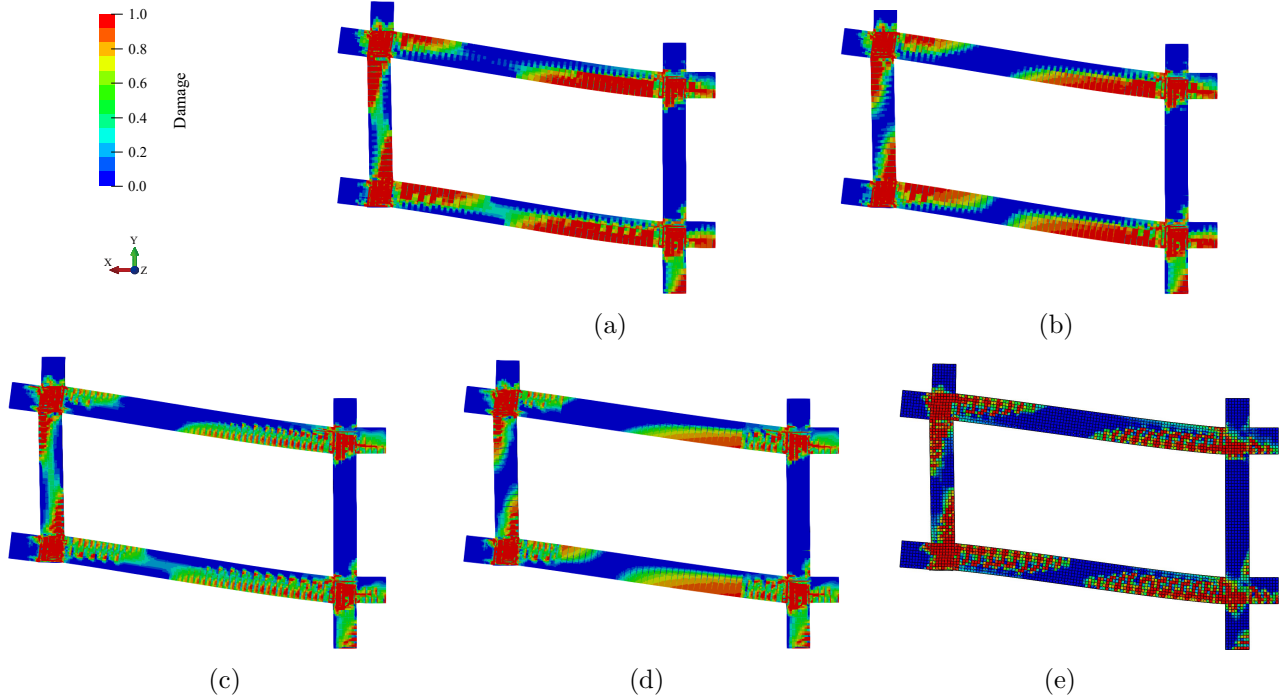


Figure 26: Damage distributions of the frame from: (a) Model 1 (Refined CW+B2); (b) Model 2 (NDK TE1+B2); (c) Model 3 (Refined CW+B3); (d) Model 4 (NDK TE1+B3); (e) ABAQUS model at the displacement of 140 mm (Scale factor is 5)

627 Regarding computational costs, Model 1 with linear elements requires more DoFs than the
 628 ABAQUS model due to the different numerical approaches utilized for reinforcements. Model
 629 1 adopts CUF models that accurately represent the actual geometry of steel components,
 630 whereas the ABAQUS model simplifies these components as 1D beam elements. Adopting
 631 similar simplifications or lower-order models for steel components may offer further reduc-
 632 tions in DoFs, enhancing the efficiency of CUF models in future developments. Nonetheless,
 633 incorporating the NDK approach saves significant computational resources, enabling Model
 634 2 to achieve a 42.3% reduction in DoFs compared to Model 1. Additionally, the DoFs needed
 635 for Model 2 are about 5% lower than those required by the ABAQUS model. While this 5%
 636 reduction may appear modest, the CUF models offer the additional advantage of providing
 637 a realistic 3D stress distribution of steel components, enhancing the models' high fidelity.
 638 Models 3 and 4 demand a considerable number of DoFs due to the use of higher-order beam

639 elements. However, applying the NDK approach in Model 4 results in approximately a 47%
640 saving in DoFs compared to Model 3. This reduction is significant given the large baseline
641 number of DoFs required by higher-order models.

642 **6 Conclusions**

643 This study presents an NDK approach for 3D global-local damage analysis of reinforced
644 concrete structures, utilizing CUF-based advanced beam models. This approach allows for
645 the application of different kinematic models at each node of the beam element. Specifically,
646 enhanced models can be generated in critical areas using Lagrange polynomials in a CW
647 manner. At the same time, lower-order refinement can be employed for the remaining regions
648 using Taylor polynomials.

649 For the validation of the proposed NDK models, four complex reinforced concrete struc-
650 tures from existing literature were selected. A modified Mazars damage model for concrete
651 and Von Mises plasticity for steel were applied to these numerical examples. The numer-
652 ical results have been compared with reference results from the literature, yielding several
653 meaningful conclusions:

- 654 1) The NDK approach optimizes beam models by combining the accuracy of local enhance-
655 ment models with the efficiency of global models, maintaining displacement continuity
656 without special coupling methods.
- 657 2) The refined CW model can accurately capture the damage behavior in RC structures,
658 even in complex scenarios such as structures with web openings or full-frame designs.
659 The NDK model demonstrates comparable performance.
- 660 3) Regarding computational resources, the NDK models reduce the DoFs by approximately
661 35% – 60% compared to the refined CW model for the previous simple cases, signifying
662 a substantial increase in computational efficiency. Notably, when the NDK models are
663 applied to the larger engineering structures, a further significant reduction in computa-
664 tional costs is anticipated.

665 4) The strong scalability of the NDK models can ensure the realization of diverse NDK
666 models by adjusting the cross-sectional kinematics at the beam element nodes as needed
667 without additional mesh discretization.

668 Reducing the refined areas in the NDK model can save computational costs at the expense
669 of model accuracy. However, defining these refined areas requires prior knowledge. Excessively
670 large refined regions can lead to insufficient savings in computing resources, whereas refined
671 areas that are too small will result in reduced model accuracy. Therefore, future work will
672 aim to find an automatic model optimization strategy based on the proposed NDK approach.
673 Furthermore, simplifying the representation of stirrups can decrease the total number of
674 required beam elements, enabling constructing a model with computational demands similar
675 to those of widely used fiber models.

676 **Data Availability Statement**

677 Some or all data, models, or code that support the findings of this study are available from
678 the corresponding author upon reasonable request.

679 **Acknowledgement**

680 This work has been partly supported by Foundation for Science and Technology, under the
681 Transitional Standard – DL57/2016/N3/UI/CERIS/CT/165/2018. The author is also grate-
682 ful for the Foundation for Science and Technology’s support through funding UIDB/04625/2020
683 from the research unit CERIS.

References

- 684
- 685 Arruda, M., Pacheco, J., Castro, L. M., and Julio, E. (2022). “A modified mazars damage
686 model with energy regularization.” *Engineering Fracture Mechanics*, 259, 108129.
- 687 Augello, R., Carrera, E., Pagani, A., Arruda, M., and Shen, J. (2023). “Node-dependent
688 kinematic models applied to reinforced concrete structures.” *Mathematics and mechanics
689 of complex systems*.
- 690 Babazadeh, A., Burgueno, R., and Silva, P. F. (2015). “Use of 3d finite-element models for
691 predicting intermediate damage limit states in rc bridge columns.” *Journal of Structural
692 Engineering*, 141(10), 04015012.
- 693 Baghi, H., Oliveira, A., Valença, J., Cavaco, E., Neves, L., and Júlio, E. (2018). “Behavior of
694 reinforced concrete frame with masonry infill wall subjected to vertical load.” *Engineering
695 Structures*, 171, 476–487.
- 696 Carrera, E., Augello, R., Pagani, A., and Xu, X. (2022). “Component-wise approach to
697 reinforced concrete structures.” *Mechanics of Advanced Materials and Structures*, 29(25),
698 3871–3888.
- 699 Carrera, E., Fiordilino, G., Nagaraj, M., Pagani, A., and Montemurro, M. (2019). “A
700 global/local approach based on cuf for the accurate and efficient analysis of metallic and
701 composite structures.” *Engineering Structures*, 188, 188–201.
- 702 Carrera, E., Giunta, G., and Petrolo, M. (2011). *Beam structures: classical and advanced
703 theories*. John Wiley & Sons, Chichester, United Kingdom.
- 704 Carrera, E., Petrolo, M., Cinefra, M., and Zappino, E. (2014). *Finite element analysis of
705 structures through unified formulation*. John Wiley & Sons, Chichester, United Kingdom.
- 706 Carrera, E. and Zappino, E. (2017). “One-dimensional finite element formulation with node-
707 dependent kinematics.” *Computers & Structures*, 192, 114–125.
- 708 Carrera, E., Zappino, E., and Li, G. (2018). “Finite element models with node-dependent
709 kinematics for the analysis of composite beam structures.” *Composites Part B: Engineering*,
710 132, 35–48.
- 711 Casanova, A., Jason, L., and Davenne, L. (2012). “Bond slip model for the simulation of
712 reinforced concrete structures.” *Engineering Structures*, 39, 66–78.

713 Ceresa, P., Petrini, L., and Pinho, R. (2007). “Flexure-shear fiber beam-column elements for
714 modeling frame structures under seismic loading—state of the art.” *Journal of Earthquake*
715 *Engineering*, 11(S1), 46–88.

716 Ceresa, P., Petrini, L., Pinho, R., and Sousa, R. (2009). “A fibre flexure–shear model for
717 seismic analysis of rc-framed structures.” *Earthquake Engineering & Structural Dynamics*,
718 38(5), 565–586.

719 Cheng, J. and Shing, P. B. (2022). “A beam-column element for modeling nonlinear flexural
720 and shear behaviors of reinforced masonry walls.” *Earthquake Engineering & Structural*
721 *Dynamics*, 51(8), 1918–1942.

722 D’Ambrisi, A. and Filippou, F. C. (1999). “Modeling of cyclic shear behavior in rc members.”
723 *Journal of Structural Engineering*, 125(10), 1143–1150.

724 de Souza Neto, E. A., Peric, D., and Owen, D. R. (2011). *Computational methods for plasticity:*
725 *theory and applications*. John Wiley & Sons, Chichester, United Kingdom.

726 Earij, A., Alfano, G., Cashell, K., and Zhou, X. (2017). “Nonlinear three–dimensional finite–
727 element modelling of reinforced–concrete beams: Computational challenges and experimen-
728 tal validation.” *Engineering Failure Analysis*, 82, 92–115.

729 Elsanadedy, H. M., Al-Salloum, Y. A., Almusallam, T. H., Alshenawy, A. O., and Abbas, H.
730 (2019). “Experimental and numerical study on frp-upgraded rc beams with large rectan-
731 gular web openings in shear zones.” *Construction and Building Materials*, 194, 322–343.

732 (2005). *EN 1992-1-1 Eurocode 2: Design of concrete structures - Part 1-1: General rules and*
733 *rules for buildings*, Brussels, Belgium. EN, CEN.

734 Feng, D.-C., Wu, G., Sun, Z.-Y., and Xu, J.-G. (2017). “A flexure-shear timoshenko fiber
735 beam element based on softened damage-plasticity model.” *Engineering Structures*, 140,
736 483–497.

737 fib special activity group (2013). *fib model code for concrete structures 2010*. Ernst & Sohn,
738 Wiley, Berlin, Germany.

739 Firmo, J. (2015). “Fire behaviour of reinforced concrete structures strengthened with cfrp
740 strips.” Ph.D. thesis, Instituto Superior Tecnico, Universidade de Lisboa, Lisbon, Portugal.

741 Firmo, J., Arruda, M., Correia, J., and Rosa, I. (2018). “Three-dimensional finite element

742 modelling of the fire behaviour of insulated rc beams strengthened with ebr and nsm cfrp
743 strips.” *Composite Structures*, 183, 124–136.

744 Girgin, S. C., Moharrami, M., and Koutromanos, I. (2018). “Nonlinear beam-based modeling
745 of rc columns including the effect of reinforcing-bar buckling and rupture.” *Earthquake
746 Spectra*, 34(3), 1289–1309.

747 Halm, D. and Dragon, A. (1996). “A model of anisotropic damage by mesocrack growth;
748 unilateral effect.” *International Journal of Damage Mechanics*, 5(4), 384–402.

749 Jirásek, M. and Bauer, M. (2012). “Numerical aspects of the crack band approach.” *Com-
750 puters & structures*, 110, 60–78.

751 Kadhim, M. M., Jawdhari, A. R., Altaee, M. J., and Adheem, A. H. (2020). “Finite element
752 modelling and parametric analysis of frp strengthened rc beams under impact load.” *Journal
753 of Building Engineering*, 32, 101526.

754 Kaleel, I., Petrolo, M., and Carrera, E. (2018). “Elastoplastic and progressive failure analy-
755 sis of fiber-reinforced composites via an efficient nonlinear microscale model.” *Aerotecnica
756 Missili & Spazio*, 97, 103–110.

757 MacGregor, J. G., Wight, J. K., Teng, S., and Irawan, P. (1997). *Reinforced concrete: Me-
758 chanics and design*, Vol. 3. Prentice Hall Upper Saddle River, NJ, New Jersey, USA.

759 Maekawa, K., Okamura, H., and Pimanmas, A. (2003). *Non-linear mechanics of reinforced
760 concrete*. CRC Press, Boca Raton, FL, USA.

761 Marini, A. and Spacone, E. (2006). “Analysis of reinforced concrete elements including shear
762 effects.” *ACI Structural Journal*, 103, 645–655.

763 Mazars, J. (1984). “Application de la mécanique de l’endommagement au comportement non
764 linéaire et à la rupture du béton de structure.” Ph.D. thesis, Université Pierre et Marie
765 Curie Paris 6, Paris, France.

766 Mullapudi, T. and Ayoub, A. (2013). “Analysis of reinforced concrete columns subjected
767 to combined axial, flexure, shear, and torsional loads.” *Journal of Structural Engineering*,
768 139(4), 561–573.

769 Murcia-Delso, J. and Benson Shing, P. (2015). “Bond-slip model for detailed finite-element
770 analysis of reinforced concrete structures.” *Journal of Structural Engineering*, 141(4),

771 04014125.

772 Nagaraj, M., Carrera, E., and Petrolo, M. (2023). “A global–local approach to the high-fidelity
773 impact analysis of composite structures based on node-dependent kinematics.” *Composite
774 Structures*, 304, 116307.

775 Nagaraj, M., Kaleel, I., Carrera, E., and Petrolo, M. (2022). “Elastoplastic micromechanical
776 analysis of fiber-reinforced composites with defects.” *Aerotecnica Missili & Spazio*, 1–7.

777 Nagaraj, M. and Maiaru, M. (2023). “Progressive damage analysis of steel-reinforced con-
778 crete beams using higher-order 1d finite elements.” *International Journal for Multiscale
779 Computational Engineering*.

780 Neuenhofer, A. and Filippou, F. C. (1997). “Evaluation of nonlinear frame finite-element
781 models.” *Journal of structural engineering*, 123(7), 958–966.

782 Ogura, N., Bolander, J. E., and Ichinose, T. (2008). “Analysis of bond splitting failure of
783 deformed bars within structural concrete.” *Engineering Structures*, 30(2), 428–435.

784 Ouyang, C., Wollrab, E., Kulkarni, S., and Shah, S. (1997). “Prediction of cracking response
785 of reinforced concrete tensile members.” *Journal of Structural Engineering*, 123(1), 70–78.

786 Petrangeli, M., Pinto, P. E., and Ciampi, V. (1999). “Fiber element for cyclic bending and
787 shear of rc structures. i: Theory.” *Journal of Engineering Mechanics*, 125(9), 994–1001.

788 Saritas, A. and Filippou, F. C. (2009). “Numerical integration of a class of 3d plastic-
789 damage concrete models and condensation of 3d stress–strain relations for use in beam
790 finite elements.” *Engineering Structures*, 31(10), 2327–2336.

791 Saritas, A. and Filippou, F. C. (2013). “Analysis of rc walls with a mixed formulation frame
792 finite element.” *Computers and Concrete*, 12(4), 519–536.

793 Scano, D., Carrera, E., and Petrolo, M. (2023). “Use of the 3d equilibrium equations in
794 the free-edge analyses for laminated structures with the variable kinematics approach.”
795 *Aerotecnica Missili & Spazio*, 1–17.

796 Shen, J., Arruda, M., Pagani, A., and Carrera, E. (2023a). “A regularized higher-order
797 beam elements for damage analysis of reinforced concrete beams.” *Mechanics of Advanced
798 Materials and Structures*, 1–13.

799 Shen, J., Arruda, M. T., and Pagani, A. (2023b). “Concrete damage analysis based on higher-

800 order beam theories using fracture energy regularization.” *Mechanics of Advanced Materials*
801 *and Structures*, 30(22), 4582–4596.

802 Shen, J., Pagani, A., Arruda, M., and Carrera, E. (2022). “Exact component-wise solutions
803 for 3d free vibration and stress analysis of hybrid steel–concrete composite beams.” *Thin-*
804 *Walled Structures*, 174, 109094.

805 Shen, J., Tiago Arruda, M. R., and Pagani, A. (2023c). “A consistent crack bandwidth for
806 higher-order beam theories: Application to concrete.” *International Journal of Damage*
807 *Mechanics*, 10567895231215557.

808 Sinaei, H., Shariati, M., Abna, A. H., Aghaei, M., and Shariati, A. (2012). “Evaluation
809 of reinforced concrete beam behaviour using finite element analysis by abaqus.” *Scientific*
810 *Research and Essays*, 7(21), 2002–2009.

811 Spacone, E., Filippou, F. C., and Taucer, F. F. (1996). “Fibre beam–column model for non-
812 linear analysis of r/c frames: Part i. formulation.” *Earthquake Engineering & Structural*
813 *Dynamics*, 25(7), 711–725.

814 Taucer, F., Spacone, E., and Filippou, F. C. (1991). *A fiber beam-column element for seis-*
815 *mic response analysis of reinforced concrete structures*, Vol. 91. Earthquake Engineering
816 Research Center, College of Engineering, University of California Berkeley.

817 Urmson, C. R. and Mander, J. B. (2012). “Local buckling analysis of longitudinal reinforcing
818 bars.” *Journal of Structural Engineering*, 138(1), 62–71.